Test of the Equivalence Principle in an Einstein Elevator

Annual Report #1

NASA Grant NAG3-2881

For the period 1 May 2003 through 28 February 2004

Principal Investigator

Irwin I. Shapiro

April 2004

Prepared for
National Aeronautics and Space Administration
Office of Biological and Physical Research
Washington, DC

Smithsonian Institution
Astrophysical Observatory
Cambridge, Massachusetts 02138

The Smithsonian Astrophysical Observatory
is a member of the
Harvard-Smithsonian Center for Astrophysics

Test of the Equivalence Principle in an Einstein Elevator

Annual Report #1

NASA Grant NAG3-2881

For the period 1 May 2003 through 28 February 2004

Principal Investigator

Irwin I. Shapiro

Co-Investigators

S. Glashow
E.C. Lorenzini
M.L. Cosmo
P.N. Cheimets
N. Finkelstein (E/PO)
M. Schneps (E/PO)

Non-US partners (IFSI)
V. Iafolla (non-US PI)
D. Lucchesi
S. Nozzoli
F. Santoli

Collaborators

J. Ashenberg

Ph.D. Students
C. Bombardelli

SAO Engineering
M. Freeman
R. Ingram

April 2004

Prepared for
National Aeronautics and Space Administration
Office of Biological and Physical Research
Washington, DC

Smithsonian Institution
Astrophysical Observatory
Cambridge, Massachusetts 02138

The Smithsonian Astrophysical Observatory
is a member of the
Harvard-Smithsonian Center for Astrophysics

Table of Contents

List of Figures

List of Tables

Introduction

The scientific goal of the experiment is to test the equality of gravitational and inertial mass (i.e., to test the Principle of Equivalence) by measuring the independence of the rate of fall of bodies from their compositions. The measurement is accomplished by measuring the relative displacement (or equivalently acceleration) of two falling bodies of different materials which are the proof masses of a differential accelerometer spinning about an horizontal axis to modulate a possible violation signal. A non-zero differential acceleration appearing at the signal frequency will indicate a violation of the Equivalence Principle. The goal of the experiment is to measure the Eötvös ratio $\delta g/g$ (differential acceleration/common acceleration) with a targeted accuracy that is about two orders of magnitude better than the state of the art (presently at several parts in 10^{13}).

The analyses carried out during this first grant year have focused on: (1) evaluation of possible shapes for the proof masses to meet the requirements on the higher-order mass moment disturbances generated by the falling capsule; (2) dynamics of the instrument package and differential acceleration measurement in the presence of errors and imperfections; (3) computation of the inertia characteristic of the instrument package that enable a separation of the signal from the dynamics-related noise; (4) a revised thermal analysis of the instrument package in light of the new conceptual design of the cryostat; (5) the development of a dynamic and control model of the capsule attached to the gondola and balloon to define the requirements for the leveling mechanism (6) a conceptual design of the leveling mechanism that keeps the capsule aligned before release from the balloon; and (7) a new conceptual design of the customized cryostat and a preliminary valuation of its cost.

The project also involves an international cooperation with the Institute of Space Physics (IFSI) in Rome, Italy. The group at IFSI is in charge of prototyping the differential accelerometer and carrying out precursor laboratory measurements. During this grant year, our partners analyzed and then designed a new prototype of differential accelerometer that has several characteristics in common with the flight accelerometer at this point of the instrument development. The highlights of these activities are documented in a section of this report.

Detector Analysis/Requirements

Conceptual design

Our partners at the Institute of Space Physics (IFSI/CNR) in Rome (Italy) have explored design options for a differential accelerometer that improves upon the present differential accelerometer prototype. The most significant change with respect to the prototype detector is that the new design allows for the pivot axes of the two proof masses to be on the same side and along a common line as shown in Figure 1 and 2. This modification is important for improving the rejection of any external force acting on the proof masses with a gradient along the detector's longitudinal axis (e.g., differential forces generated by a rotational acceleration perpendicular to the longitudinal axis).

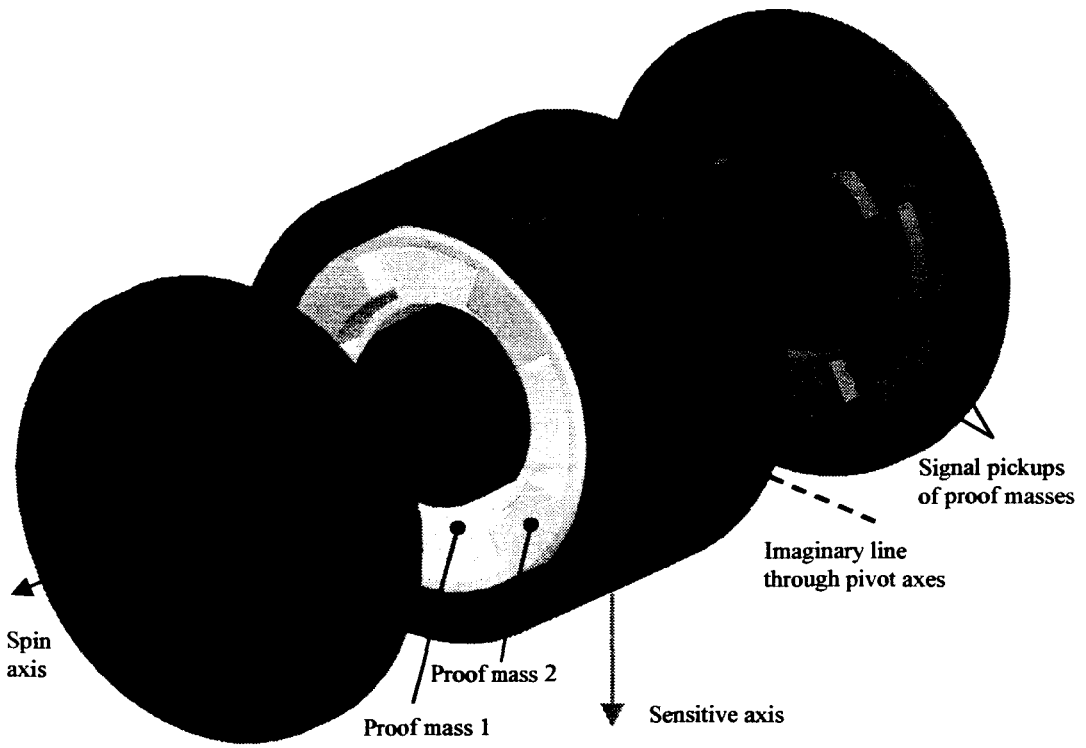

Figure 1 Example of new conceptual design of differential accelerometer

The inner sensing mass (mass 1) is attached with two torsional pivots to the internal core of the instrument while the outer sensing mass (mass 2) is attached to the external cylindrical component of the instrument (see Figure 2). This arrangement enables the independent machining of each proof mass, its internal (or external) support and pivots.

Subsequently, the two units can be assembled into the final configuration by sliding one inside the other and locking them in place by means of the signal pick-up disks on both sides.

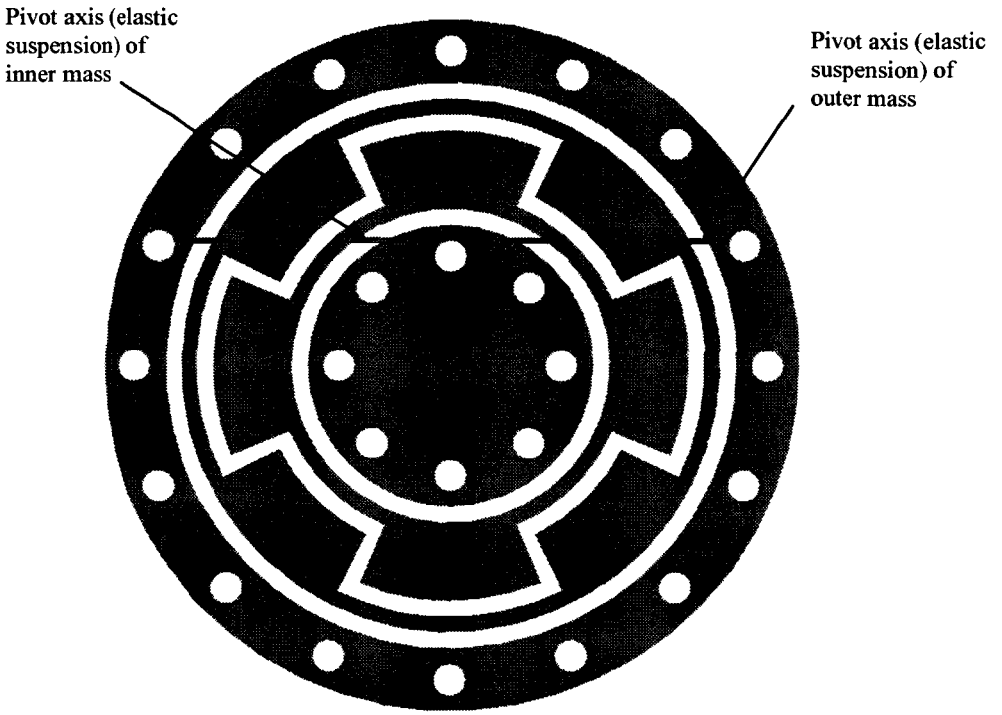

Figure 2 Cross section of proof-masses showing their pivot axes

The shape of the test masses is dictated by geometrical and gravitational constraints which will be addressed in detail in the next section. They can be toothed-cylinders as shown in Figure 1 and 2 or simply hollow cylinders (without teeth) but with specific ratios between their radii and lengths as computed in the following section. Either geometry can meet the gravitational requirements stemming from the higher-order mass moments produced by the capsule but there are other considerations related to the construction of the proof masses and the pickup plates. For these reasons we will explore both geometries leaving the two options open for future refinements.

Analysis of Test Bodies Geometrical Design

Requirements and Constraints

The goal of the analysis is to find geometrical solutions to a set of constraints aimed at obtaining the desired gravitational and dynamical behavior of the proof masses. A primary constraint is to attain a spherical inertia ellipsoid (of the second-order inertia moments) for the two sensing masses. A second constraint is for the two sensing masses to have the same moment of inertia with respect to their (coincident) pivot axes. The latter constraint enables the two masses to respond equally to a common-mode perturbation. The two proof masses do not need to have the same physical mass but they need to move by the same amount about the pivot axis which is guaranteed by the equality of the moments of inertia about the pivot axis (i.e. the proof masses need to have the same "effective" mass).

In the following discussion we will analyze and define a feasible shape for the test bodies. We are constrained by the general topology shown in figure 1: each body is a cut of a cylinder, with a cross-section consisting of a ring and four teeth (or without teeth). The outer body has an outside ring while the inner body has an inside ring. The teeth-contours are arcs and radials. The gap between the bodies is very small compared with the size of the body's cross-section. Both bodies are connected by a pivot axis located at some offset from the center and passing through the axial line.

There are some heuristics constraints such that the radius of the inner hole should be small but not too small, the arc lengths of the teeth, for each body, should not be too different. The rings do not have to be of the same thickness, but they have to be wide enough due to elementary structural considerations. The bodies have different mass density. Contrary to the geometrical variables, the densities are pre-determined. The inner body has the higher density. We will consider two density ratios: 7.8 (Platinum/Aluminum pair) and 3.3 (Copper/Aluminum pair)

Our goal is to construct a manifold of feasible geometrical parameters subject to the following strong constraints:

C1: $Ixx_1 = Iyy_1 = Izz_1$

C2: $Ixx_2 = Iyy_2 = Izz_2$

C3: $Iy'y'_1 = Iy'y'_2 \quad \Rightarrow \quad Iyy_1 + M_1b^2 = Iyy_2 + M_2b^2$

where x is along the longitudinal symmetry axis, y is through the center of mass and parallel to the pivot axis (y') while z is orthogonal to x and y.

The first two constraints: equal moments of inertia for each body, is the realization of the requirement of nulling the MacCullagh's gravitational perturbation. These constraints construct manifolds that are function of the geometrical parameters. On the other hand, the third constraint manifold is a function of the density ratio as well. The

constraint requires equal moment of inertia with respect to the pivot, and its realization if due to the Sterling formula for translation of moments if inertia.

There is a soft constraint on the length ratio and on the mass ratio. Both should be as close to one as feasible, especially the length ratio.

There are 9 free parameters: 7 geometrical and 2 mass densities. By normalizing each length by the outer radius, and by considering only the density ratio, we reduce the number of free parameters to 7:

$$\gamma_1, \widetilde{R}_1 = R_1 / R_0, \widetilde{\delta}_1 = \delta_1 / R_0, \widetilde{\delta}_2 = \delta_2 / R_0, \widetilde{\varepsilon} = \varepsilon / R_0, \widetilde{\rho} = \rho_1 / \rho_2, \widetilde{b} = b / R_0$$

Since there are more free parameters (7) than constraints (3), the feasible solution is on a 4-dimension manifold. Accordingly, the method of having a feasible solution is either to pre-determine 4 parameters or to pre-determine some m parameters (m < 4) and to define 4-m objective functions to be minimized. Candidates for such objective functions are $(L1/L2-1)^2$ and $(M1/M2-1)^2$.

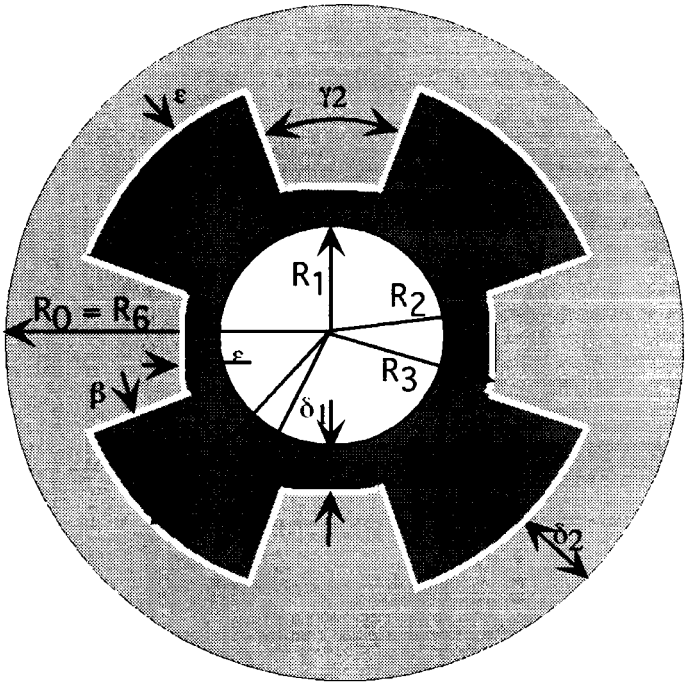

Figure 3 A Cross-section of test bodies geometry

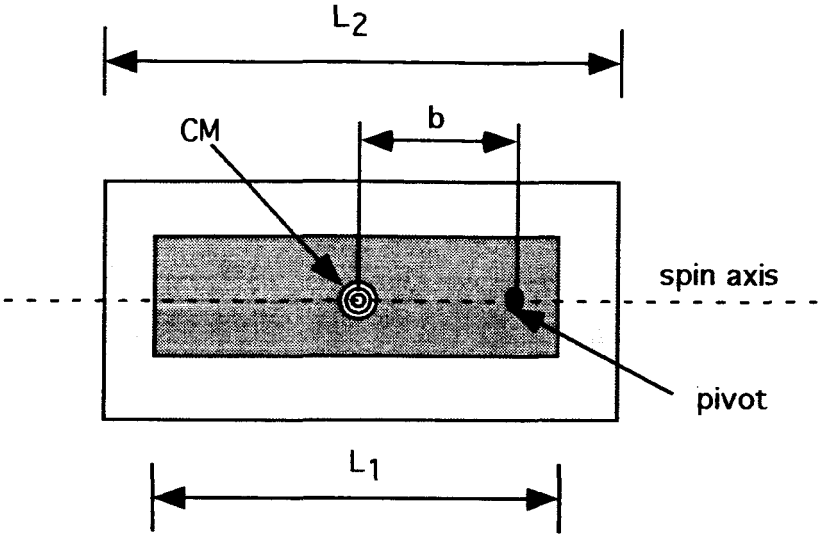

Figure 4 Side-view of test bodies geometry

Geometrical Analysis

The cross-section of each test body consists of two types of shapes: rings and teeth. The desired shape is a combination of both. In order to understand the contribution of each shape, we will investigate the limiting cases: cylindrical and teeth-like test bodies. Once we compute the characteristics of the limiting shapes we can easily construct the characteristics of the proposed bodies. In the following we will denote the inner and outer bodies by the subscripts 1 and 2, respectively.

Cylindrical Test Bodies

Given two concentric bodies; the inner radius of body 1 is R_i, and the outer radius of body 2 is R_O. R_m is the outer radius of body 1 and the inner radius of body 2.

The masses and the moments of inertia of the two test bodies are:

$$M_1 = \pi\rho_1 L_1(\tilde{R}_m^2 - \tilde{R}_i^2)$$

$$M_1 = \pi\rho_1 L_2(\tilde{R}_O^2 - \tilde{R}_m^2)$$

$$Ixx_1 = \frac{1}{2}M_1(R_i^2 + R_m^2)$$

$$Iyy_1 = Izz_1 = \frac{1}{12}M_1[L_1^2 + 3(R_i^2 + R_m^2)]$$

$$Ixx_2 = \frac{1}{2}M_2(R_m^2 + R_O^2)$$

$$Iyy_2 = Izz_2 = \frac{1}{12} M_2 [L_2^{\,2} + 3(R_m^{\,2} + R_O^{\,2})]$$

The equal moments of inertia constraints lead to the following length ratio and mass ratios:

$$C1,C2: \quad L_1 = \sqrt{3}\sqrt{R_i^{\,2} + R_m^{\,2}} \quad , L_2 = \sqrt{3}\sqrt{R_m^{\,2} + R_O^{\,2}} \quad \Rightarrow \quad \frac{L_2}{L_1} = \sqrt{\frac{1+\tilde{R}_m^2}{\tilde{R}_i^2 + \tilde{R}_m^2}} \quad \Rightarrow \quad \frac{L_2}{L_1} > 1$$

$$\frac{M_1}{M_2} \overset{C_1,C_2}{=} \frac{\rho_1}{\rho_2}\sqrt{\frac{\tilde{R}_i^2 + \tilde{R}_m^2}{1+\tilde{R}_m^2}\,\frac{\tilde{R}_m^2 - \tilde{R}_i^2}{1-\tilde{R}_m^2}}$$

The pivot constraint leads to the following mass ratio:

$$C3: \quad \frac{M_1}{M_2} = \frac{1+\tilde{R}_m^2 + 2\tilde{b}^{\,2}}{\tilde{R}_i^2 + \tilde{R}_m^2 + 2\tilde{b}^{\,2}} \quad \Rightarrow \quad \frac{M_1}{M_2} > 1 \quad ; \quad (\tilde{b} \le \frac{\sqrt{3}}{2}\sqrt{\tilde{R}_i^2 + \tilde{R}_m^2})$$

The meaning of the inequality on the pivot location is that it should be on the shorter body, otherwise the pivot would not go through the shorter body (see Figure 4). The above results show that in the case of cylindrical bodies, the inner body should be shorter with bigger mass. Equal length bodies would not satisfy the constraints. In addition, the inner body results to be heavier than the outer body.

Teeth-like Test Bodies

The mass of the inner body is: $M_1 = 2\gamma_1 \rho_1 (R_O^{\,2} - R_i^{\,2}) L_1$. Since $\gamma_2 = 0.5\pi - \gamma_1$ then the mass of the outer body is: $M_2 = (\pi - 2\gamma_1)\rho_2 (R_O^{\,2} - R_i^{\,2}) L_2$.

The resulting moments of inertia are:

$$Ixx_1 = \gamma\, \rho\, L_1 (R_O^4 - R_i^4)$$

$$Iyy_1 (= Izz_1) = \frac{1}{6}\gamma_1\, \rho_1\, L_1 (R_O^2 - R_i^2)[L_1^{\,2} + 3(R_O^2 + R_i^2)]$$

Note that in the computation of Iyy_1 we evaluated the following integral as

$$\int_{\theta \in \Gamma} \cos^2\theta \; d\theta = 2\gamma$$

where Γ is the set of the teeth arcs:

$$\Gamma = \{[-\frac{\gamma}{2},\frac{\gamma}{2}],[\frac{\pi}{2}-\frac{\gamma}{2},\frac{\pi}{2}+\frac{\gamma}{2}],[\pi-\frac{\gamma}{2},\pi+\frac{\gamma}{2}],[\frac{3\pi}{2}-\frac{\gamma}{2},\frac{3\pi}{2}-\frac{\gamma}{2}]\}$$

The moments of inertia in terms of the body mass are:

$$Ixx_1 = \frac{1}{2}M_1(R_O{}^2 + R_i{}^2)$$

$$Iyy_1 = Izz_1 = \frac{1}{12}M_1[L^2 + 3(R_O{}^2 + R_i{}^2)]$$

The corresponding moments of inertia of the outer body are:

$$Ixx_2 = \frac{1}{2}M_2(R_O{}^2 + R_i{}^2)$$

$$Iyy_2 = Izz_2 = \frac{1}{12}M_2[L_2{}^2 + 3(R_O{}^2 + R_i{}^2)]$$

The equal moments of inertia constraints result in equal lengths:

$$C1,C2: \quad L_1 = \sqrt{3}\sqrt{R_i{}^2 + R_O{}^2} \quad , L_2 = \sqrt{3}\sqrt{R_i{}^2 + R_O{}^2} \quad \Rightarrow \quad L_1 = L_2$$

Since both bodies should have the same length, the pivot constraint leads to equal masses:

$$C3: \quad (M_1 - M_2)\underbrace{[L^2 + 3(R_i{}^2 + R_O{}^2) + 12b^2]}_{0} = 0 \quad \Rightarrow \quad M_1 = M_2 \quad \Rightarrow \quad \gamma_1 = \frac{\pi}{2(1+\frac{\rho_1}{\rho_2})}$$

Note that *if* $\rho_1 = \rho_2 \quad \Rightarrow \quad \gamma_1 = \gamma_2 = \frac{1}{4}\pi$.

Combined Cylinders and Teeth

The mass and the moments of inertia can be easily computed based on the previous cases. First, the radii of the configuration are related as follows:

$$R_1 = R_i$$
$$R_2 = R_i + \delta_1$$
$$R_3 = R_i + \delta_1 + \varepsilon$$
$$R_4 = R_O - \delta_2 - \varepsilon$$
$$R_5 = R_O - \delta_2$$
$$R_6 = R_O$$

Let B_1 and B_2 denotes the inner and the outer body, respectively. Then, the angular quantities are:

$$\gamma_1 \in B_1, \gamma_2 = \frac{\pi}{2} - \gamma_1 - 2\beta \in B_2, \beta = \frac{\varepsilon}{(R_2 + R_5)/2} \notin \{B_1, B_2\}$$

We divided each body into a cylindrical part (B_{11}, B_{22}) and a part consisting of teeth (B_{12}, B_{21}), described by the following functional relations:

$$B_{11}(R_1, R_2, \frac{\pi}{2}) + B_{12}(R_2, R_4, \gamma_1) \rightarrow B_1(r_1, r_2, \gamma)$$

$$B_{21}(R_3, R_5, \gamma_2) + B_{22}(R_5, R_6, \frac{\pi}{2}) \rightarrow B_2(r_1, r_2, \gamma)$$

The masses and the moments of inertia are:

$$M_1 = \underbrace{\pi \rho_1 L_1 (R_2^2 - R_1^2)}_{M_{11}} + \underbrace{2\gamma_1 \rho_1 L_1 (R_4^2 - R_2^2)}_{M_{12}}$$

$$M_2 = \underbrace{2\gamma_2 \rho_2 L_2 (R_5^2 - R_3^2)}_{M_{21}} + \underbrace{\pi \rho_2 L_2 (R_6^2 - R_5^2)}_{M_{22}}$$

$$Ixx_1 = \frac{1}{2}[M_{11}R_1^2 + M_1 R_2^2 + M_{12}R_4^2]$$
$$Iyy_1 = Izz_1 = \frac{1}{12}[M_1 L_1^{\,2} + 3M_{11}R_1^2 + 3M_1 R_2^2 + 3M_{12}R_4^2]$$
$$Ixx_2 = \frac{1}{2}[M_{21}R_3^2 + M_2 R_5^2 + M_{22}R_6^2]$$
$$Iyy_2 = Izz_2 = \frac{1}{12}[M_2 L_2^{\,2} + 3M_{21}R_3^2 + 3M_2 R_5^2 + 3M_{22}R_6^2]$$

The equal moments of inertia constraints result in the following lengths:

$$C1: \quad L_1 = \sqrt{3}\sqrt{\widetilde{M}_{11}\widetilde{R}_1^2 + \widetilde{R}_2^2 + \widetilde{M}_{12}\widetilde{R}_4^2}$$

$$C2: \quad L_2 = \sqrt{3}\sqrt{\widetilde{M}_{21}\widetilde{R}_3^2 + \widetilde{R}_5^2 + \widetilde{M}_{22}}$$

where

$$\widetilde{M}_{11} = \frac{\pi(\widetilde{R}_2^2 - \widetilde{R}_1^2)}{\pi(\widetilde{R}_2^2 - \widetilde{R}_1^2) + 2\gamma_1(\widetilde{R}_4^2 - \widetilde{R}_2^2)}$$

$$\widetilde{M}_{12} = \frac{2\gamma_1(\widetilde{R}_4^2 - \widetilde{R}_2^2)}{\pi(\widetilde{R}_2^2 - \widetilde{R}_1^2) + 2\gamma_1(\widetilde{R}_4^2 - \widetilde{R}_2^2)}$$

$$\widetilde{M}_{21} = \frac{2\gamma_2(\widetilde{R}_5^2 - \widetilde{R}_3^2)}{\pi(1 - \widetilde{R}_5^2) + 2\gamma_2(\widetilde{R}_5^2 - \widetilde{R}_3^2)}$$

$$\widetilde{M}_{22} = \frac{\pi(1 - \widetilde{R}_5^2)}{\pi(1 - \widetilde{R}_5^2) + 2\gamma_2(\widetilde{R}_5^2 - \widetilde{R}_3^2)}$$

In order to validate the consistency of the results we will examine the limiting cases.

When the bodies are cylinders:

$$R_1 = R_i, R_2 = R_m, R_3 = R_m, R_4 = R_5, R_5 = R_m, M_{11} = M_1, M_{12} = 0, M_{21} = 0, M_{22} = M_2$$

The lengths are:

$$L(C1) = \sqrt{3}\sqrt{R_i^2 + R_m^2}\ , \quad L(C2) = \sqrt{3}\sqrt{R_m^2 + R_O^2}$$

When the bodies are teeth only:

$$R_1 = R_i, R_2 = R_i, R_3 = R_i, R_4 = R_O, R_5 = R_O, M_{11} = 0, M_{12} = M_1, M_{21} = M_2, M_{22} = 0$$

The lengths are:

$$L(C1) = \sqrt{3}\sqrt{R_i^2 + R_O^2} \ = \ L(C2) = \sqrt{3}\sqrt{R_i^2 + R_O^2}$$

Therefore, the results are consistent with the limiting cases.

The issue that we will investigate now is the possibility of equal lengths. As we already proved, there are equal lengths in the case of teeth-bodies, but not in the case of cylindrical bodies. It is intuitive to conclude that the inner body is always shorter than the outer body. However, we will prove it formally.

A necessary condition for length equality is that

$$\exists\ \{\widetilde{M}_{11},\widetilde{M}_{12},\widetilde{M}_{21},\widetilde{M}_{22}) \quad \text{such that} \quad \underbrace{\widetilde{M}_{11}\widetilde{R}_1^2+\widetilde{R}_2^2+\widetilde{M}_{12}\widetilde{R}_4^2}_{\Psi_1} \geq \underbrace{\widetilde{M}_{21}\widetilde{R}_3^2+\widetilde{R}_5^2+\widetilde{M}_{22}}_{\Psi_2}$$

(Because it is easy to see that $\exists\ \{\widetilde{M}_{11},\widetilde{M}_{12},\widetilde{M}_{21},\widetilde{M}_{22})$ such that $\Psi_1 < \Psi_2$)

But if $\Psi_1 \geq \Psi_2$ then $\max \Psi_1 > \min \Psi_2$

It is easy to prove that $\underset{\{M_{11},M_{12}\}}{\arg\max}\,\Psi_1 = \{0,1\}$ and $\underset{\{M_{21},M_{22}\}}{\arg mim}\,\Psi_2 = \{1,0\}$

But $\widetilde{R}_3 > \widetilde{R}_2$ and $\widetilde{R}_5 > \widetilde{R}_4 \Rightarrow \widetilde{R}_2^2+\widetilde{R}_4^2 < \widetilde{R}_3^2+\widetilde{R}_5^2$

And $\Psi_1 < \widetilde{R}_2^2+\widetilde{R}_4^2$, $\Psi_2 > \widetilde{R}_3^2+\widetilde{R}_5^2$

Therefore $L(C1) < L(C2)$

The last constraint is:

$$C3: \quad \Phi = \frac{M_1}{M_2}\underbrace{(\widetilde{M}_{11}\widetilde{R}_1^2+\widetilde{R}_2^2+\widetilde{M}_{12}\widetilde{R}_4^2)}_{\Psi_1} - \underbrace{(\widetilde{M}_{21}\widetilde{R}_3^2+\widetilde{R}_5^2+\widetilde{M}_{22})}_{\Psi_2} + \underbrace{\frac{1}{3}[\frac{M_1}{M_2}(\widetilde{L}_1^{\,2}+12\widetilde{b}^{\,2})-(\widetilde{L}_2^{\,2}+12\widetilde{b}^{\,2})]}_{\Psi_3} = 0$$

This constraint involves the mass densities. So we are looking for possible geometry and mass ratio that satisfies the constraint. The formal proof for the feasibility of parameters is presented as follows.

We already proved that $L_1 \leq L_2$ (the equality is for a teeth-only bodies).

Therefore

if $\frac{M_1}{M_2} \leq 1 \Rightarrow \Psi_3 \leq 0$

but $\Psi_1 < \Psi_2 \Rightarrow \frac{M_1}{M_2}\Psi_1 - \Psi_2 < 0 \Rightarrow \Phi < 0$

But

else if $\frac{M_1}{M_2} >> 1 \Rightarrow \Psi_3 > 0$ and $\frac{M_1}{M_2}\Psi_1 > \Psi_2$

$\Rightarrow \exists \frac{M_1}{M_2}$ such that $\Phi = 0$

In summary, we proved that the first two constraints require that $L_1 \le L_2$, and that there is a set of parameters that includes the condition $M_1 > M_2$ that satisfies the third constraint.

Numerical Results

The goal of the numerical investigation is to find a feasible set of parameters, i.e. parameters that satisfy the hard constraint as well as the soft constraints. The method is to fix few parameters, to compute the manifold that satisfies the hard constraints, and to choose the set of free parameters that best satisfy the soft constraint.

The considerations of choosing the fixed parameters are due to the design requirements and the constraint sensitivity. The considerations are as follows. The gap between the two bodies should be small, the cylindrical hole should be wide enough but not too large, and the pivot should be close to the end of the inner body. In addition, these three are the least sensitive parameters. The value of these parameters was chosen as: $\widetilde{\varepsilon} = 0.01, \widetilde{R}_i = 0.2, b = 0.9(L_1/2)$. In general, the influence of the offset b is as follows. A smaller offset require the moments if inertia to be close to each other ($Iyy_1 \approx Iyy_2$), while a larger offset requires the masses to be close to each other ($M_1 \approx M_2$). The difficulty here is when the mass-density ratio is big and the offset is large. In order to constraint the mass difference one should narrow the teeth-angle of the heavier mass. This is the reason why the configuration with a smaller mass-density ratio is expected to be a better one.

We investigated the feasible configurations for two mass-density ratios: 3.3 (Cooper/Aluminum) and 7.8 (Platinum/Aluminum). The method of solution is to solve constraint C3 for γ_1 given δ_1, δ_2, and then compute the associated M_1/M_2 and L_1/L_2. The following matrices show these parameters computed on a grid of δ_1, δ_2, for the two density ratios (where δ_1 and δ_2 are the thickness of the inner and outer rings, respectively).

The configuration with $\rho_1 / \rho_2 = 3.3$ yields:

$$\delta_2 \rightarrow$$

$$\delta_1 \downarrow \underbrace{\begin{bmatrix} 0.3683 & 0.4534 & 0.5664 & 0.7198 & 0.9339 \\ 0.3649 & 0.4504 & 0.5640 & 0.7183 & 0.9334 \\ 0.3596 & 0.4452 & 0.5591 & 0.7141 & 0.9303 \\ 0.3515 & 0.4367 & 0.5504 & 0.7056 & 0.9231 \\ 0.3393 & 0.4233 & 0.5359 & 0.6907 & 0.9093 \end{bmatrix}}_{\gamma_1}$$

$$\delta_1, \delta_2 = \{0., 0.05, 0.1, 0.15, 0.2\}$$

$$\Downarrow$$

$$\underbrace{\left[\begin{bmatrix} 1.0106 & 1.0774 & 1.1608 & 1.2682 & 1.4125 \\ 1.0544 & 1.1202 & 1.2017 & 1.3057 & 1.4435 \\ 1.1078 & 1.1718 & 1.2506 & 1.3498 & 1.4793 \\ 1.1705 & 1.2319 & 1.3066 & 1.3996 & 1.5188 \\ 1.2420 & 1.2995 & 1.3688 & 1.4539 & 1.5609 \end{bmatrix}\right]}_{\frac{M_1}{M_2}} \Rightarrow \underbrace{\left[\begin{bmatrix} 0.9884 & 0.9240 & 0.8587 & 0.7920 & 0.7229 \\ 0.9447 & 0.8887 & 0.8314 & 0.7722 & 0.7102 \\ 0.8985 & 0.8511 & 0.8019 & 0.7506 & 0.6965 \\ 0.8520 & 0.8128 & 0.7717 & 0.7284 & 0.6821 \\ 0.8069 & 0.7753 & 0.7419 & 0.7062 & 0.6678 \end{bmatrix}\right]}_{\frac{L_1}{L_2}}$$

The configuration with $\rho_1 / \rho_2 = 7.8$ yields:

$$\delta_2 \rightarrow$$

$$\delta_1 \downarrow \underbrace{\begin{bmatrix} 0.1808 & 0.2226 & 0.2779 & 0.3526 & 0.4557 \\ 0.1770 & 0.2189 & 0.2744 & 0.3493 & 0.4529 \\ 0.1717 & 0.2131 & 0.2681 & 0.3425 & 0.4456 \\ 0.1634 & 0.2036 & 0.2571 & 0.3298 & 0.4310 \\ 0.1505 & 0.1882 & 0.2387 & 0.3078 & 0.4049 \end{bmatrix}}_{\gamma_1} \qquad \delta_1, \delta_2 = \{0., 0.05, 0.1, 0.15, 0.2\}$$

$$\Downarrow$$

$$\underbrace{\begin{bmatrix} 1.0106 & 1.0671 & 1.1347 & 1.2168 & 1.3183 \\ 1.0996 & 1.1546 & 1.2198 & 1.2984 & 1.3945 \\ 1.2075 & 1.2595 & 1.3207 & 1.3939 & 1.4826 \\ 1.3319 & 1.3794 & 1.4349 & 1.5008 & 1.5798 \\ 1.4705 & 1.5118 & 1.5599 & 1.6164 & 1.6834 \end{bmatrix}}_{\frac{M_1}{M_2}} \Rightarrow \underbrace{\begin{bmatrix} 0.9884 & 0.9330 & 0.8776 & 0.8220 & 0.7658 \\ 0.9051 & 0.8631 & 0.8201 & 0.7760 & 0.7305 \\ 0.8277 & 0.7969 & 0.7646 & 0.7308 & 0.6952 \\ 0.7591 & 0.7371 & 0.7137 & 0.6886 & 0.6616 \\ 0.6998 & 0.6846 & 0.6681 & 0.6502 & 0.6307 \end{bmatrix}}_{\frac{L_1}{L_2}}$$

When $\delta_1 = \delta_2 = 0$, the teeth-only configuration has a unity mass ratio and a unity length ratio. (The ratios are not exactly one because $\varepsilon \quad 0$). The mass and length ratios are more sensitive to δ_2 than to δ_1. Some good feasible values of δ_1, δ_2 are marked (for mass-density ratio of 3.3) by enlarged numbers. The higher density ratio (7.9) results in inferior configuration. In particular, the teeth-angle of the heavier mass is narrower, and the length ratio is lower.

A special set is the parametric set corresponding to $\gamma_1 = \gamma_2$. The following table shows a few representatives cases for this case. The mass density ratio is 3.3. Note that u. ually $\delta_1 < \delta_2$, although there is a unique solution for $\delta_1 = \delta_2$ (the last row). Moreover, γ_2 is always constant. Also note that the teeth-angles are a bit different between the cases. The reason is due to the small gap between the teeth.

δ_1	δ_2	γ_1	γ_2	M_1 / M_2	L_1 / L_2
0.05	0.1629	0.7670	0.7670	1.3375	0.7565
0.1	0.1641	0.7678	0.7678	1.3828	0.7356
0.15	0.1664	0.7685	0.7685	1.4351	0.7136
0.1674	0.1674	0.7687	0.7687	1.4549	0.7058

The plot below shows a visualization of the feasible manifolds of γ_1, M_1/M_2 and L_1/L_2, for the two density ratios. (Feasible parameters are parameters that satisfy the hard constraint and, the desirable parameters are a subgroup of this set that is bound by the soft constraints).

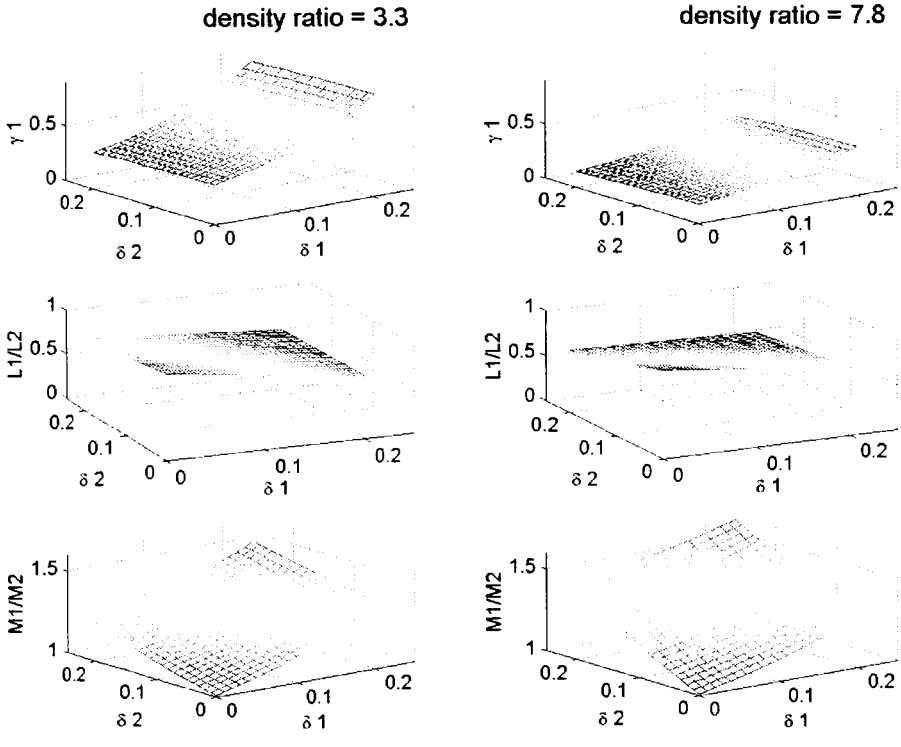

Figure 5 Feasible parameters for $\rho_1/\rho_2 = 3.3$ and $\rho_1/\rho_2 = 7.8$

Design Case and Validation

We present here a realization of the case $\rho_1/\rho_2 = 3.3$ where $\tilde{\delta}_1 = 0.1$ and $\tilde{\delta}_2 = 0.1641$.

The non-dimensional solution is:

$\tilde{R}_1 = 0.2, \tilde{R}_2 = 0.3, \tilde{R}_3 = 0.31, \tilde{R}_4 = 0.826, \tilde{R}_5 = 0.836, \tilde{R}_6 = 1$ and $\gamma_1 = \gamma_2 = 0.7678$ rad.

Given an outer radius of 5cm, the dimensions become:

$R_1 = 1\,[cm]$

$R_2 = 1.5\,[cm]$

$R_3 = 1.55\,[cm]$

$R_4 = 4.13\,[cm]$

$R_5 = 4.18\,[cm]$

$R_6 = 5\,[cm]$

$L_1 = 7.13\,[cm]$

$L_2 = 9.69\,[cm]$

$b = 0.9 \cdot (0.5L_1) = 3.2\,[cm]$

$M_1 = 1.72\,[kg]$

$M_2 = 1.25\,[kg]$

We validated the resulting configuration by computing the moments of inertia, and the moment if inertia with respect to the pivot, for the recommended configuration.

The inertia coefficients of the second-order for body 1 are:

$Jxx = 1.435x10^{-3}, Jyy = Jzz = 1.435x10^{-3}\,[kg - m^2]$

The inertia coefficients of the second-order for body 2 are:

$Jxx = 1.915x10^{-3}, Jyy = Jzz = 1.915x10^{-3}\,[kg - m^2]$

Therefore, the moments of inertia of each body with respect to its center of mass are equal.

The moments of inertia with respect to the pivot are:

$Iyy_1 + M_1 b^2 = 3.169x10^{-3}, Iyy_2 + M_2 b^2 = 3.169x10^{-3}\ [kg - m^2]$

Therefore, the moments of inertia with respect to the pivot are the same for the two bodies.

Although the above configuration satisfies the inertia constraint, it should also be checked for gravitational perturbations. A part of the design, defined by the first two constraints, is the cancellation of the second-order gravitational perturbations. The symmetry cancelled the first-order as well as the third-order. So the leading term of the gravitational perturbations is the forth-order.

The inertia coefficients of the forth-order for body 2 are:

$$Jxxxx = 1.6x10^{-6}, Jyyyy = Jzzzz = 1.4x10^{-6}, Jxxyy = Jxxzz = 8x10^{-7}, Jyyzz = 3.9x10^{-7}\ [kg - m^4]$$

We computed the gravitational lateral force on body 2 at a representative location (half way through a worst-case free-fall trajectory) inside the capsule. Note that the forces on body 1 are much smaller due of its smaller dimension.

The following plot shows the lateral accelerations on body 2 for a complete cycle, and the corresponding frequency spectrum. The first harmonic (P1) is in the order of $3x10^{-15}\ [m/s^2]$ which is an acceptable gravitational perturbation for this experiment.

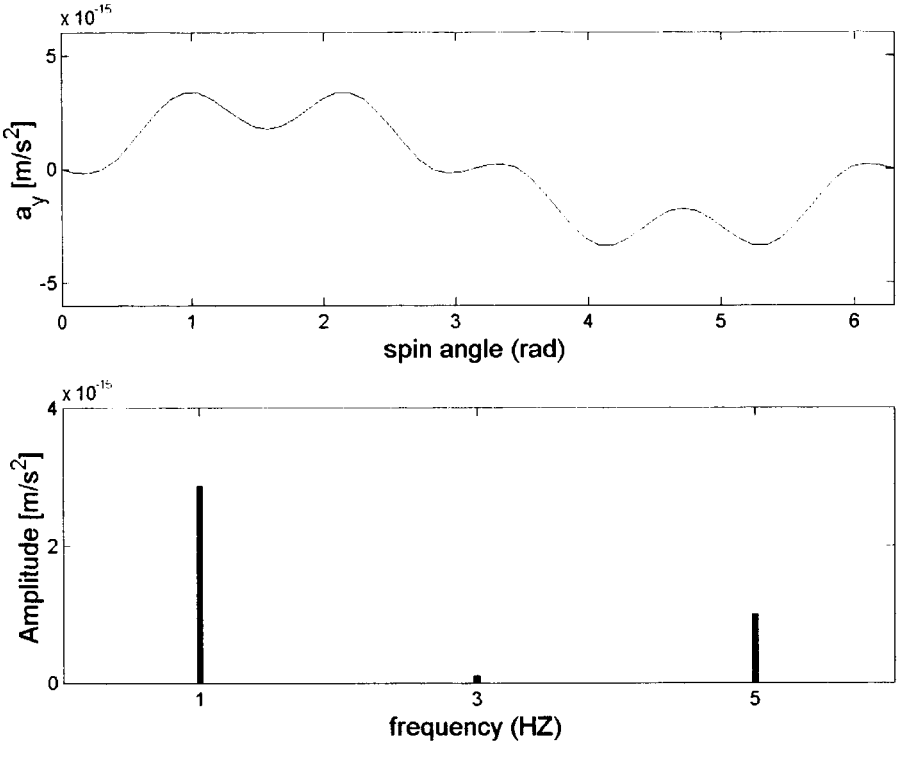

Figure 6 Lateral Acceleration of fourth-order due to Capsule Attraction

Concluding Remarks

We found a feasible set of geometrical parameters that satisfy the design constraints on the test bodies. The hard constraints are the equality of the moments of inertia for each body and the equality of the moments of inertia with respect to the pivot. The soft constraints are that the mass ratio of the two bodies and especially the length ratio should

be close to one. In addition, the values of the teeth angles of the two bodies should be close. There are seven design (free) parameters. The results are mostly sensitive to only three parameters: teeth angle and the widths of the inner and the outer rings. We examined the results for two possible mass-density ratios: 3.3 and 7.8 corresponding to Copper/Aluminum and Platinum/Aluminum.

Our analysis indicates that it is preferable to use the lower mass-density ratio. Inner ring width of 0.05-0.1 and outer ring width of 0.1-0.15 (normalized by the outer radius) will give a mass ratio of 1.2-1.35 and a length ratio of 0.75-0.83, for an inner body teeth angle of 0.56-0.72 radians. (Note that the ideal teeth angle is $2\pi/8 = 0.78$ radians). Thinner rings will make these ratios closer to one. We also computed some representative cases for equal teeth angles, and a unique case for equal teeth angles as well as equal ring widths. In particular, we examined a configuration with $\widetilde{\delta}_1 = 0.1$ and the corresponding $\widetilde{\delta}_2 = 0.1641$ for equal teeth angles, and adopted it as our design configuration. We concluded, through numerical verification, that the design configuration satisfies the design constraints. In addition, we confirmed that the gravitational perturbation acting on these bodies is acceptable.

Instrument package and detector dynamics

The dynamics model that was developed during the previous grant NAG8-1780 (see Ref. [1]) for the instrument package and detector used 6 degrees of freedom (DOF) for each rigid body in the system. The model was instrumental in computing the eigenfrequencies, eigenvectors, and in simulating the dynamics of a few specific cases. The analysis led to the selection of the 3-body configuration over the 2-body configuration based on the ability of the former in a better rejection of perturbations acting on the outer shell of the instrument package. Moreover, eigenfrequencies of the 3-body detector were selected in such a way that the two eigenfrequencies, corresponding to the common and differential modes of the sensing masses along the measurement axis, are much lower than any other elastic eigenfrequency in the system. The model captures many details of the detector dynamics but it is CPU intensive, tedious to run and not suitable for parametric analysis.

Since most eigenfrequencies are orders of magnitude higher than the eigenfrequencies directly affecting the measurement, most degrees of freedoms can be safely neglected without affecting the motion along the measurement axis. This consideration leads to the conclusion that only those DOFs that are dominant in the low-frequency eigenvectors need to be retained. Specifically, we will build a fast-execution model that has the three rotational degrees of freedom of the whole instrument package and the two motional degrees of freedom of the proof masses along the sensitive axis.

For all cases, the displacements of the sensing masses with respect to the instrument package are miniscule. This condition implies that the angular momentum vectors of all the bodies are parallel and also that terms of second order or higher of the relative displacements can be neglected in the equations of motion. In the derivation of the equations of motions we assume that the centers of mass of the three bodies do not coincide in order to account for mass distribution errors. We also include the dominant external forces acting on the proof masses and the instrument package.

Translational equations of motion

Let us consider a set of three rigid bodies A,B,C constrained to each other in such a way that their relative motion is a translation along the sensitive axis x. Let A and B be linked with C through a spring dashpot system characterized by elastic and damping coefficients (k_A, ξ_A) and (k_B, ξ_B) respectively. A and B are the proof masses while C is the case of the instrument package. Let the central symmetry axes of the three bodies be parallel to one another.

Let x,y,z be a body reference frame centered at the global center of mass CM of the system composed by the three rigid bodies, with x along the relative motion of the three bodies, z the central symmetry axis and y right-handed with z and x. Given the mutual translation constraint A,B,C have the same angular rotation vector: $\boldsymbol{\omega}_A = \boldsymbol{\omega}_B = \boldsymbol{\omega}_C = \boldsymbol{\omega} = (\omega_x, \omega_y, \omega_z)^T$.

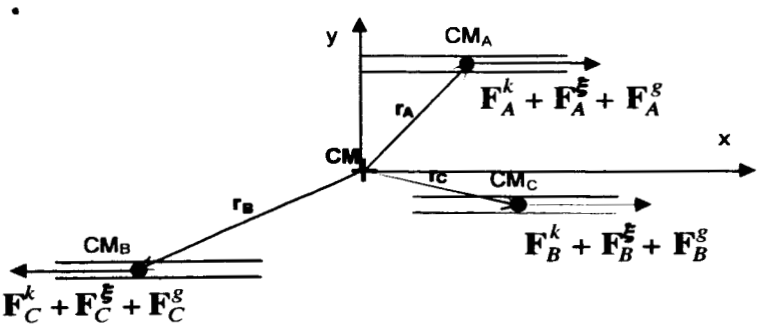

Figure 7 Schematic of individual centers of mass position with respect to the system center of mass. Relative motion takes place along the x axis.

The equations of motion of the system written with respect to an inertial system centered at the Earth are:

$$m_A(\ddot{\mathbf{R}}_{CM} + \ddot{\mathbf{r}}_A^I) = \mathbf{F}_A^g + \mathbf{F}_A^k + \mathbf{F}_A^\xi \tag{1.1}$$

$$m_B(\ddot{\mathbf{R}}_{CM} + \ddot{\mathbf{r}}_B^I) = \mathbf{F}_B^g + \mathbf{F}_B^k + \mathbf{F}_B^\xi \tag{1.2}$$

$$m_C(\ddot{\mathbf{R}}_{CM} + \ddot{\mathbf{r}}_C^I) = \mathbf{F}_C^g + \mathbf{F}_C^k + \mathbf{F}_C^\xi \tag{1.3}$$

where $\mathbf{r}$ is the radius vector of each individual center of mass relative to the combined CM of the system, $\mathbf{R}_{CM}$ is the radius vector of CM to the Earth center, $\mathbf{F}^g$ is the Earth gravity force, $\mathbf{F}^k$ the internal spring force and $\mathbf{F}^\xi$ the internal damping force acting on each mass and the derivatives are computed with respect to the inertial frame.

The gravitational forces for each mass can be written in terms of a gravity gradient tensor Γ^E with respect to CM and the acceleration of the CM as follows:

$$\mathbf{F}_A^g = m_A\left(\ddot{\mathbf{R}}_{CM} + \Gamma^E \mathbf{r}_A\right) \tag{2.1}$$

$$\mathbf{F}_B^g = m_B\left(\ddot{\mathbf{R}}_{CM} + \Gamma^E \mathbf{r}_B\right) \tag{2.2}$$

$$\mathbf{F}_C^g = m_C\left(\ddot{\mathbf{R}}_{CM} + \Gamma^E \mathbf{r}_C\right) \tag{2.3}$$

By choosing the inertial frame such that the Y axis is parallel to $\mathbf{R}_{CM}$, the Earth gravity gradient matrix has the simple form:

$$\Gamma^E = \frac{GM_E}{R_{CM}^3}\begin{bmatrix} -1 & 0 & 0 \\ 0 & 2 & 0 \\ 0 & 0 & -1 \end{bmatrix}$$

After plugging Eqs (2) into Eqs (1) we obtain:

$$\ddot{\mathbf{r}}_A^I = \mathbf{\Gamma}^E \mathbf{r}_A + \frac{\mathbf{F}_A^k + \mathbf{F}_A^\xi}{m_A} \tag{3.1}$$

$$\ddot{\mathbf{r}}_B^I = \mathbf{\Gamma}^E \mathbf{r}_B + \frac{\mathbf{F}_B^k + \mathbf{F}_B^\xi}{m_B} \tag{3.2}$$

$$\ddot{\mathbf{r}}_C^I = \mathbf{\Gamma}^E \mathbf{r}_C + \frac{\mathbf{F}_C^k + \mathbf{F}_C^\xi}{m_C} \tag{3.3}$$

The above equations can be written with respect to the body reference frame x,y,z as follows:

$$\ddot{\mathbf{r}}_A + [\dot{\boldsymbol{\omega}}]\mathbf{r}_A + [\boldsymbol{\omega}][\boldsymbol{\omega}]\mathbf{r}_A + 2[\boldsymbol{\omega}]\dot{\mathbf{r}}_A = \mathbf{\Gamma}_{xyz}^E \mathbf{r}_A + \frac{\mathbf{F}_A^k + \mathbf{F}_A^\xi}{m_A} \tag{4.1}$$

$$\ddot{\mathbf{r}}_B + [\dot{\boldsymbol{\omega}}]\mathbf{r}_B + [\boldsymbol{\omega}][\boldsymbol{\omega}]\mathbf{r}_B + 2[\boldsymbol{\omega}]\dot{\mathbf{r}}_B = \mathbf{\Gamma}_{xyz}^E \mathbf{r}_B + \frac{\mathbf{F}_B^k + \mathbf{F}_B^\xi}{m_B} \tag{4.2}$$

$$\ddot{\mathbf{r}}_C + [\dot{\boldsymbol{\omega}}]\mathbf{r}_C + [\boldsymbol{\omega}][\boldsymbol{\omega}]\mathbf{r}_C + 2[\boldsymbol{\omega}]\dot{\mathbf{r}}_C = \mathbf{\Gamma}_{xyz}^E \mathbf{r}_C + \frac{\mathbf{F}_C^k + \mathbf{F}_C^\xi}{m_C} \tag{4.3}$$

where $\mathbf{r}_A, \mathbf{r}_B, \mathbf{r}_C$ are the radius vectors of each individual center of mass relative to CM and the derivatives are now computed with respect to the body frame.

R_{IB}, R_{BI} = rotation matrixes from the inertial X,Y,Z to the x,y,z body frame and vice versa while $[\omega] = R_{IB}\dot{R}_{BI}$ is the angular velocity matrix of frame x,y,z

The gravity gradient tensor in the body reference frame becomes (see later on):

$$\mathbf{\Gamma}_{xyz}^E = R_{IB}\mathbf{\Gamma}^E R_{BI} = \begin{bmatrix} g_{xx} & g_{xy} & g_{xz} \\ g_{xy} & g_{yy} & g_{yz} \\ g_{xz} & g_{yz} & g_{zz} \end{bmatrix} \tag{5}$$

At this point we will express Eqs (4) in terms of the stretches x_A, x_B of the springs linking A with C and B with C.

Let $\mathbf{r}_{A0}, \mathbf{r}_{B0}, \mathbf{r}_{C0}$ be the radius vectors of the individual center of masses with respect to CM when the springs are at rest. We can write

$$\mathbf{r}_A = \mathbf{r}_{A0} + \zeta_A \mathbf{u}_x = [r_{A0x} + \zeta_A, r_{A0y}, r_{A0z}]^T \tag{6.1}$$

$$\mathbf{r}_B = \mathbf{r}_{B0} + \zeta_B \mathbf{u}_x = [r_{B0x} + \zeta_B, r_{B0y}, r_{B0z}]^T \tag{6.2}$$

$$\mathbf{r}_C = -m_A/m_C(\mathbf{r}_{A0} + \zeta_A \mathbf{u}_x) - m_B/m_C(\mathbf{r}_{B0} + \zeta_B \mathbf{u}_x) \tag{6.3}$$

where the ζ are the stretches of the springs measured from the combined CM and the definition of CM has been used to derive eqn. (6.3).

From Eq. (6.3) $\mathbf{r}_C$ can be expressed as:

$$\mathbf{r}_C = \mathbf{r}_{C0} - 1/m_C\,(\,m_A\zeta_A + m_B\zeta_B)\,\mathbf{u}_x \tag{7}$$

with

$$\mathbf{r}_{C0} = -1/m_C\,(m_A\,\mathbf{r}_{A0} + m_B\,\mathbf{r}_{B0}) \tag{8}$$

Let $\boldsymbol{\delta}_A$, $\boldsymbol{\delta}_B$ be error position vectors from the center of mass of C to the center of mass of A and B, respectively, when the springs are at rest. We have:

$$\boldsymbol{\delta}_A = \mathbf{r}_{A0} - \mathbf{r}_{C0} = \mathbf{r}_{A0}(1+m_A/m_C) + \mathbf{r}_{B0}\,m_B/m_C \tag{9.1}$$

$$\boldsymbol{\delta}_B = \mathbf{r}_{B0} - \mathbf{r}_{C0} = \mathbf{r}_{B0}(1+m_B/m_C) + \mathbf{r}_{A0}\,m_A/m_C \tag{9.2}$$

We can now compute the total stretches x_A, x_B (as opposed to the partial stretches with respect to the CM) of the two springs linking A with C and B with C as follows:

$$x_A = (r_{Ax} - r_{A0x}) - (r_{Cx} - r_{C0x}) = \zeta_A(1 + m_A/m_C) + \zeta_B\,m_B/m_C \tag{10.1}$$

$$x_B = (r_{Bx} - r_{B0x}) - (r_{Cx} - r_{C0x}) = \zeta_B(1 + m_B/m_C) + \zeta_A\,m_A/m_C \tag{10.2}$$

Solving Eq. (9) for $\mathbf{r}_{A0}$, $\mathbf{r}_{B0}$ and Eq. (10) for ζ_A, ζ_B yields:

$$\mathbf{r}_{A0} = \boldsymbol{\delta}_A(m_B+m_C)/m_T - \boldsymbol{\delta}_B\,m_B/m_T \tag{11.1}$$

$$\mathbf{r}_{B0} = \boldsymbol{\delta}_B(m_A+m_C)/m_T - \boldsymbol{\delta}_A\,m_A/m_T \tag{11.2}$$

$$\zeta_A = x_A(m_B+m_C)/m_T - x_B\,m_B/m_T \tag{11.3}$$

$$\zeta_B = x_B(m_A+m_C)/m_T - x_A\,m_A/m_T \tag{11.4}$$

We can now write the equations of relative motion of the centers of mass of A and B with respect to C in terms of the total spring stretches $x_A(t)$ and $x_B(t)$:

$$\ddot{\mathbf{r}}_A + [\dot{\boldsymbol{\omega}}]\mathbf{r}_A + [\boldsymbol{\omega}][\boldsymbol{\omega}]\mathbf{r}_A + 2[\boldsymbol{\omega}]\dot{\mathbf{r}}_A = \boldsymbol{\Gamma}^E_{xyz}\mathbf{r}_A - \left(\frac{k_A}{m_A}x_A + \frac{\xi_A}{m_A}\dot{x}_A\right)\mathbf{u}_x \tag{12.1}$$

$$\ddot{\mathbf{r}}_B + [\dot{\boldsymbol{\omega}}]\mathbf{r}_B + [\boldsymbol{\omega}][\boldsymbol{\omega}]\mathbf{r}_B + 2[\boldsymbol{\omega}]\dot{\mathbf{r}}_B = \boldsymbol{\Gamma}^E_{xyz}\mathbf{r}_B - \left(\frac{k_B}{m_B}x_B + \frac{\xi_B}{m_B}\dot{x}_B\right)\mathbf{u}_x \tag{12.2}$$

$$\mathbf{r}_C = -\frac{m_A}{m_C}\mathbf{r}_A - \frac{m_B}{m_C}\mathbf{r}_B \tag{12.3}$$

with

$$\mathbf{r}_A = \boldsymbol{\delta}_A(m_B+m_C)/m_T - \boldsymbol{\delta}_B m_B/m_T + (x_A(m_B+m_C)/m_T - x_B m_B/m_T)\mathbf{u}_x \tag{13.1}$$

$$\mathbf{r}_B = \boldsymbol{\delta}_B(m_A+m_C)/m_T - \boldsymbol{\delta}_A m_A/m_T + (x_B(m_A+m_C)/m_T - x_A m_A/m_T)\mathbf{u}_x \tag{13.2}$$

while eqn. (12.3) simply expresses the fact that the position of the CM of body C is defined by the position of the combined CM.

After substituting Eqs. (13) into Eqs. (12) and considering the x components only (i.e., along the sensitive axis of the accelerometer) of Eqs. (12) we obtain the translational equations of the proof masses with respect to C as follows:

$$\begin{aligned}&\ddot{x}_A - \left(\omega_y^2 + \omega_z^2 - g_{xx}\right)x_A + \frac{k_A}{m_{AC}}x_A + \frac{k_B}{m_C}x_B + \frac{\xi_A}{m_{AC}}\dot{x}_A + \frac{\xi_B}{m_C}\dot{x}_B + \\ &+\left[\left(\dot{\omega}_y - g_{xz}\right)\delta_{Az} - \left(\dot{\omega}_z + g_{xy}\right)\delta_{Ay} + \left(\omega_z\delta_{Az} + \omega_y\delta_{Ay}\right)\omega_x - \left(\omega_z^2 + \omega_y^2 - g_{xx}\right)\delta_{Ax}\right] = 0\end{aligned} \tag{14.1}$$

$$\begin{aligned}&\ddot{x}_B - \left(\omega_y^2 + \omega_z^2 - g_{xx}\right)x_B + \frac{k_B}{m_{BC}}x_B + \frac{k_A}{m_C}x_A + \frac{\xi_B}{m_{BC}}\dot{x}_B + \frac{\xi_A}{m_C}\dot{x}_A + \\ &+\left[\left(\dot{\omega}_y - g_{xz}\right)\delta_{Bz} - \left(\dot{\omega}_z + g_{xy}\right)\delta_{By} + \left(\omega_z\delta_{Bz} + \omega_y\delta_{By}\right)\omega_x - \left(\omega_z^2 + \omega_y^2 - g_{xx}\right)\delta_{Bx}\right] = 0\end{aligned} \tag{14.2}$$

Attitude equations of motion

The attitude equations of motion of the instrument package can be derived based on the conservation of angular momentum. Let [I] be the global inertia matrix of the system with respect to CM. Assuming that the three bodies have their inertia matrix diagonal with respect to the body frame x,y,z, the global inertia matrix can be written as:

$$[I] = \begin{bmatrix} I_{xx}(t) & 0 & 0 \\ 0 & I_{yy}(t) & 0 \\ 0 & 0 & I_{zz}(t) \end{bmatrix} \tag{15}$$

with

$$I_{xx}(t) = I_{xx}^A + I_{xx}^B + I_{xx}^C + m_A(r_{Ay}^2 + r_{Az}^2) + m_B(r_{By}^2 + r_{Bz}^2) + m_C(r_{Cy}^2 + r_{Cz}^2) \tag{16.1}$$

$$I_{yy}(t) = I_{yy}^A + I_{yy}^B + I_{yy}^C + m_A(r_{Ax}^2 + r_{Az}^2) + m_B(r_{Bx}^2 + r_{Bz}^2) + m_C(r_{Cx}^2 + r_{Cz}^2) \tag{16.2}$$

$$I_{zz}(t) = I_{zz}^{A} + I_{zz}^{B} + I_{zz}^{C} + m_A(r_{Ax}^{\ 2} + r_{Ay}^{\ 2}) + m_B(r_{Bx}^{\ 2} + r_{By}^{\ 2}) + m_C(r_{Cx}^{\ 2} + r_{Cy}^{\ 2}) \tag{16.3}$$

The conservation of angular momentum in body axes yields:

$$\frac{d}{dt}\{H\} = [\dot{I}]\{\omega\} + [\omega][I]\{\omega\} + [I]\{\dot{\omega}\} = \{\tau\} \tag{17}$$

where the symbol { } stands for column vector, {H} is the angular momentum vector, $\{\omega\} = [\omega_x\ \omega_y\ \omega_z]^T$ the angular velocity vector, $\{\dot{\omega}\}$ the angular acceleration and $\{\tau\}$ is the external torque vector. After substituting eqns. (12) into eqns. (17), computing the derivative, eqn. (17) yields the attitude equations of the instrument package as follows:

$$\begin{aligned}
&\left[m_A\frac{m_B+m_C}{m_T}\left(\delta_{Ay}^2+\delta_{Az}^2\right)-2m_A\frac{m_B}{m_T}\left(\delta_{Ay}\delta_{By}+\delta_{Az}\delta_{Bz}\right)+\right.\\
&\left.m_B\frac{m_A+m_C}{m_T}\left(\delta_{By}^2+\delta_{Bz}^2\right)+I_{xx}\right]\dot{\omega}_x+\\
&\left[m_A\frac{m_B+m_C}{m_T}\left(\delta_{Ay}^2-\delta_{Az}^2\right)-2m_A\frac{m_B}{m_T}\left(\delta_{Ay}\delta_{By}-\delta_{Az}\delta_{Bz}\right)+\right.\\
&\left.m_B\frac{m_A+m_C}{m_T}\left(\delta_{By}^2-\delta_{Bz}^2\right)+\left(I_{zz}-I_{yy}\right)\right]\omega_y\omega_z=\tau_x
\end{aligned} \tag{18.1}$$

$$\left\{m_A\frac{m_B+m_C}{m_T}\left(\delta_{Ax}^2+\delta_{Az}^2\right)-2m_A\frac{m_B}{m_T}\left(\delta_{Ax}\delta_{Bx}+\delta_{Az}\delta_{Bz}\right)+m_B\frac{m_A+m_C}{m_T}\left(\delta_{Bx}^2+\delta_{Bz}^2\right)+\right.$$

$$2m_A\left[\frac{m_B+m_C}{m_T}\delta_{Ax}-m_B\delta_{Bx}\right]x_A+2m_B\left[\frac{m_A+m_C}{m_T}\delta_{Bx}-m_A\delta_{Ax}\right]x_B+I_{yy}\Big\}\dot{\omega}_y+$$

$$2m_A\left[\frac{m_B+m_C}{m_T}\delta_{Ax}-m_B\delta_{Bx}\right]\omega_y\dot{x}_A+2m_B\left[\frac{m_A+m_C}{m_T}\delta_{Bx}-m_A\delta_{Ax}\right]\omega_y\dot{x}_B+$$

$$2m_A\left[\frac{m_B}{m_T}\delta_{Bx}-\frac{m_B+m_C}{m_T}\delta_{Ax}\right]\omega_x\omega_z x_A+2m_B\left[\frac{m_A}{m_T}\delta_{Ax}-\frac{m_A+m_C}{m_T}\delta_{Bx}\right]\omega_x\omega_z x_B+$$

$$\left[m_A\frac{m_B+m_C}{m_T}\left(\delta_{Az}^2-\delta_{Ax}^2\right)-2m_A\frac{m_B}{m_T}\left(\delta_{Az}\delta_{Bz}-\delta_{Ax}\delta_{Bx}\right)+\right.$$

$$\left.m_B\frac{m_A+m_C}{m_T}\left(\delta_{Bz}^2-\delta_{Bx}^2\right)+\left(I_{xx}-I_{zz}\right)\right]\omega_x\omega_z=\tau_y \tag{18.2}$$

$$\left\{m_A\frac{m_B+m_C}{m_T}\left(\delta_{Ax}^2+\delta_{Ay}^2\right)-2m_A\frac{m_B}{m_T}\left(\delta_{Ax}\delta_{Bx}+\delta_{Ay}\delta_{By}\right)+m_B\frac{m_A+m_C}{m_T}\left(\delta_{Bx}^2+\delta_{By}^2\right)+\right.$$

$$2m_A\left[\frac{m_B+m_C}{m_T}\delta_{Ax}-m_B\delta_{Bx}\right]x_A+2m_B\left[\frac{m_A+m_C}{m_T}\delta_{Bx}-m_A\delta_{Ax}\right]x_B+I_{zz}\Big\}\dot{\omega}_z+$$

$$2m_A\left[\frac{m_B+m_C}{m_T}\delta_{Ax}-m_B\delta_{Bx}\right]\omega_z\dot{x}_A+2m_B\left[\frac{m_A+m_C}{m_T}\delta_{Bx}-m_A\delta_{Ax}\right]\omega_z\dot{x}_B+$$

$$2m_A\left[\frac{m_B+m_C}{m_T}\delta_{Ax}-\frac{m_B}{m_T}\delta_{Bx}\right]\omega_x\omega_y x_A+2m_B\left[\frac{m_A+m_C}{m_T}\delta_{Bx}-\frac{m_A}{m_T}\delta_{Ax}\right]\omega_x\omega_y x_B+$$

$$\left[m_A\frac{m_B+m_C}{m_T}\left(\delta_{Ax}^2-\delta_{Ay}^2\right)-2m_A\frac{m_B}{m_T}\left(\delta_{Ax}\delta_{Bx}-\delta_{Ay}\delta_{By}\right)+\right.$$

$$\left.m_B\frac{m_A+m_C}{m_T}\left(\delta_{Bx}^2-\delta_{By}^2\right)+\left(I_{yy}-I_{xx}\right)\right]\omega_x\omega_y=\tau_z \tag{18.3}$$

where $m_{AC}=\dfrac{m_A\cdot m_C}{m_A+m_C}$, $m_{BC}=\dfrac{m_B\cdot m_C}{m_B+m_C}$, $m_T = m_A + m_B + m_C$ is the total mass of the instrument package.

Euler angles

One possibility to describe the attitude of the instrument package is through Euler angles ϕ, θ, ψ. We adopt the rotational sequence 2-1-3 because it leads to relatively simple formulas for the external torques in body axes for a body spinning about an horizontal axis and also avoid the trigonometric discontinuity. The physical significance of the angles in the 2-1-3 sequence with the Y inertial axis along the local vertical are ϕ = azimuth, θ = elevation and ψ = spin. The Euler angular rates are related to the rotational velocities ω_x, ω_y and ω_z through the following equations:

$$\begin{aligned}
\dot{\phi} &= \left(\omega_y \cos\psi + \omega_x \sin\psi\right)/\cos\theta \\
\dot{\theta} &= \omega_x \cos\psi - \omega_y \sin\psi \\
\dot{\psi} &= \omega_z + \left(\omega_y \cos\psi + \omega_x \sin\psi\right)\tan\theta
\end{aligned} \tag{19}$$

which after integration provide the Euler angles.

We now derive the key disturbances acting on the free-falling instrument package. For properly designed sensing masses in which the higher-order mass moments have all been made negligible, the Earth's gravity gradient is the most important force perturbation. After considering the rotational matrix of the Euler sequence 2-1-3, eqn

$$\mathbf{R}_{IB}^{2-1-3} = \begin{bmatrix} c\psi c\phi + s\psi s\theta s\phi & s\psi c\theta & -c\psi s\phi + s\psi s\theta c\phi \\ -s\psi c\phi + c\psi s\theta s\phi & c\psi c\theta & s\psi s\phi + c\psi s\theta c\phi \\ c\theta s\phi & -s\theta & c\theta c\phi \end{bmatrix} \tag{20}$$

Eqn. (5) holds all the components of the gravity gradient tensor in body reference frame. In eqn. (20), c stands for cosine and s for sine. For our purposes we are only interested in the first column of the tensor, whose components are:

$$\begin{aligned}
g_{xx} &= \frac{GM}{R^3}\left[-\left(c\psi c\phi + s\psi s\theta s\phi\right)^2 + 2\left(s\psi c\theta\right)^2 + \left(-c\psi s\phi + s\psi s\theta c\phi\right)^2\right] \\
g_{xy} &= \frac{GM}{R^3}\left[\left(c\psi c\phi + s\psi s\theta s\phi\right)\left(s\psi c\phi - c\psi s\theta s\phi\right) + 2s\psi c\psi\left(c\theta\right)^2 + \right. \\
&\qquad \left.\left(c\psi s\phi - s\psi s\theta c\phi\right)\left(s\psi s\phi + c\psi s\theta c\phi\right)\right] \\
g_{xz} &= \frac{GM}{R^3}\left[-c\theta s\phi\left(c\psi c\phi + s\psi s\theta s\phi\right) - 2s\psi c\theta s\theta + c\theta c\phi\left(c\psi s\phi - s\psi s\theta c\phi\right)\right]
\end{aligned} \tag{21}$$

We also add a WEP violation signal to the motion equation of proof mass A in order to test in the dynamics simulation the ability to extract a small signal out of the dynamics-generated noise. If we assume that the WEP violation signal acts on proof mass A only, then its projection along the sensitive axis of the accelerometer is:

$$a_{Ax}^{EPV} = (\sin\psi\cos\theta)a^{EPV} \tag{21}$$

where a^{EPV} is the strength of the differential violation signal.

The proof masses will have spherical inertia ellipsoids (barring construction errors) and, consequently, the gravity torques acting on them will be negligible. On the contrary, the instrument package must have an axisymmetric yet non-spherical inertia ellipsoid in order to separate the frequencies of the dynamic noise (related to the precession frequency) from the signal frequency of a possible EP violation. A body with non-spherical inertia will be subjected to gravity gradient torques which will modulate slightly its precession dynamics. Consequently, we include in the rotational equations of the instrument package the gravity-gradient disturbance torques which are given by:

$$\begin{aligned}
\tau_x &= 3\frac{GM}{R^3}(I_z - I_y)nm \\
\tau_y &= 3\frac{GM}{R^3}(I_z - I_x)nl \\
\tau_z &= 3\frac{GM}{R^3}(I_x - I_y)lm
\end{aligned} \tag{22}$$

After computing the direction cosines *l, m, n* in the body reference frame through the 2-1-3 rotation sequence, we obtain:

$$\begin{aligned}
\tau_x &= -3\frac{GM}{R^3}(I_z - I_y)\cos\psi\cos\theta\sin\theta \\
\tau_y &= -3\frac{GM}{R^3}(I_z - I_x)\sin\psi\cos\theta\sin\theta \\
\tau_x &= 3\frac{GM}{R^3}(I_x - I_y)\sin\psi\cos\psi\cos^2\theta
\end{aligned} \tag{23}$$

In this model the two proof masses translates along the x-axis (sensitive axis) without rotating about the pivot axis as it would be the case for proof mass suspensions that are off the CMs of the proof masses. This is a simplification that is justified by the very small displacements of the proof masses and it is an adequate approximation at this level of analysis and instrument development. Off-centered pivots will not necessarily lead to detrimental effects because these effects will likely appear at the precession frequency and its multiples and not at the signal frequency. Nevertheless, a more complete model of the differential accelerometer that reflects these additional dynamic coupling is being developed and it will be used to run additional computer simulations in parallel to the maturing of the flight accelerometer.

Numerical results

The translational and rotational equations of motion have been solved numerically by using a IV-order, variable step size, Runge-Kutta numerical integrator after checking the routine for accuracy on dynamic cases with known solutions.

A large number of simulations were run with the goal of identifying suitable system parameters and check the tolerance to construction imperfections and errors at release. We adopted the following values for masses and spring stiffnesses as a reference case that falls within the acceptable values of sizes and masses of the proof masses:

Masses

$m_A = 1$ kg

$m_B = 1$ kg

$m_C = 30$ kg

Moments of inertia (about CM) of proof masses

$I_{AX} = I_{AY} = I_{AZ} = 7.75 \times 10^{-4}$ kg-m^2

$I_{BX} = I_{BY} = I_{BZ} = 7.75 \times 10^{-4}$ kg-m^2

The instrument package has been assumed as an axisymmetric body. Its moments of inertia have been varied from simulation to simulation in order to shift the precession frequency and its multiples with respect to the signal frequency (i.e., the spin frequency) and analyze its effects on the signal. An EP violation signal at a threshold value has been included in the simulations. A random white noise with a noise amplitude higher than the signal is added in some simulations to the differential output signal in order to simulate the intrinsic noise components of the accelerometer (Brownian noise and amplifier noise).

The output of the accelerometer is a differential displacement between the two proof masses (i.e., the quantity measured by the accelerometer pickup system). The input acceleration is then retrieved from the output displacement signal through the transfer function of the accelerometer. The spectrum of the differential acceleration (or analogously the differential displacement) consists of: harmonics related to the elastic vibrations of the proof masses; noise peaks at multiple frequencies related to the precession dynamics of the instrument package; other harmonics related to the gravity gradient components of the Earth; the EP violation signal (appearing at the spin frequency) and, if added, a white noise. The goal is to extract the signal out of this multi-faceted noise spectrum. A key element is the selection of the moments of inertia of the instrument package in order to provide a clear separation between signal and dynamics-related noise frequencies.

We start the analysis by looking at features of the attitude dynamics of the free-falling package. For this purpose, we assume that the CM of proof mass 1 is displaced from the other two bodies (proof mass 2 and the instrument package) by the expected tolerance of 1 micron. We also assume errors at release that will force the instrument package to precess according to its inertia characteristics.

A cylindrically-symmetric instrument package with its highest moment of inertia along the spin axis will exhibit a retrograde precession (opposite to the spin) with a body-precession frequency higher than the spin frequency. An instrument package with the minimum moment of inertia along the spin axis will exhibit a prograde precession (in the same direction of the spin) with a body-precession frequency lower than the spin frequency.

We have explored several combinations of ratios of moments of inertia with the goal of keeping the precession-related acceleration frequencies separate from the signal frequency (that is the spin frequency). The precession dynamics of the three-body system results in several frequencies showing up in the differential acceleration output that are multiple of the fundamental precession frequency of the instrument package.

It would be tempting at first look to use a retrograde precession in order to shift all the precession-dynamic-related harmonics to frequencies higher than the spin frequency. There are, however, other limitations because the strength of the precession-related harmonics depend on the frequency itself and its relationship with respect to the spin frequency. This statement is explained better by looking at the formula for the acceleration along the sensitive axis x (measured on board the body) of a single precessing body that was derived in Ref. [ii] and it is reported here for completeness with the z-axis along the spin axis:

$$a_x = -\omega_t(\nu - \Omega)\cos(\Omega t)\delta_y + \frac{1}{2}\omega_t^2 \sin(2\Omega t)\delta_z + \left[\nu^2 + \frac{1}{2}\omega_t^2(1+\cos(2\Omega t))\right]\delta_x \qquad (24)$$

In equation (24), ν is the spin rate, Ω is the body-axis precession rate, ω_t is the error velocity at release (orthogonal to the spin rate) and δ_x, δ_y, δ_z are the displacement errors between the point where the acceleration is measured (it can be thought as the CM of a proof mass) and the CM of the instrument package.

The amplitude of the first term, which is modulated at the precession frequency Ω, is proportional to $\nu - \Omega$ Consequently, the amplitude of this term is minimized if the precession frequency is prograde and not far away from the spin frequency. On the contrary, the term becomes large for retrograde precession because the two frequencies add up in this case.

After assuming realistic values of release and geometrical errors, the amplitude of the term (at the precession frequency) is typically several order of magnitude bigger than the threshold signal. For this reason the term can easily overpower the signal nearby. Conversely, if the precession frequency is well separated from the spin frequency and, especially if the precession is retrograde, this acceleration term can become strong

enough to saturate the dynamic range of the accelerometer. In conclusion, there is a window of precession frequencies that enable an extraction of a threshold signal from noise without saturating the accelerometer response as it will be shown better in the numerical results. In anticipation of those results, the convenient precession frequency window, in terms of the spin frequency, is:

$$0.4\nu \leq \Omega \leq 0.6\nu \tag{25}$$

where the body-axis precession frequency is given by:

$$\Omega = \frac{I_t - I_z}{I_t}\nu \tag{26}$$

In eqn. (26) I_z is the moment of inertia about the symmetry axis (which ideally coincides with spin axis) and I_t is the moment of inertia about the transverse axis of the axisymmetric body.

The spin frequency is also bound by upper and lower limits. The lower limit is defined by the need to have a sufficient numbers of spin cycles during the measurement time. The upper limit is defined by the accelerometer saturation due to the instrument package dynamics (related to centrifugal forces) combined with the proof masses centering errors. After carrying out a few trials, a convenient window for the spin rate is between 0.4 Hz and 1 Hz. In the following work we have adopted $\nu \leq 0.5$ Hz which is less taxing on the centering requirements of the accelerometer with respect to the instrument package CM because a slower rotation rate produces smaller centrifugal forces on sensing masses with centering errors.

In the following simulations we have adopted errors as follows:

Centering errors of proof mass A with respect to C: $\delta_{Ax} = \delta_{Ay} = \delta_{Az} = 10$ micron;

Centering errors of proof mass B with respect to C: $\delta_{Bx} = \delta_{By} = \delta_{Bz} = 11$ micron;

Initial displacement of proof masses at release = 50 microns;

Transverse angular rate error at release: $\omega_t = 0.1$ deg/s;

Angle at release between symmetry axis of detector and horizontal plane = 0.1 deg.

The initial transient oscillations at release are abated by reducing the high Q value of the detector (through feedback dissipation) to Q = 2. After 5 s devoted to damping, the feedback control is removed and the measurement phase starts with a Q of order 10^5. This damping and switch logic is included in the simulation in order to provide a realistic representation of the damping process after release.

Signal extraction (preliminary)

Before going into the details of the parametric analysis, we will point out briefly the noise extraction technique that has been used so far. As pointed out previously, the noise produced by elastic and precession dynamics is a colored noise at known frequencies. The problem is that the strengths of these harmonics are several orders of magnitude higher than the signal strength and, consequently, a simple spectral analysis is not enough to resolve the signal.

The approach that has been followed thus far is to fit accurately (with a least square technique) the accelerometer output with sinusoidal functions, starting from the dominant and lowest-frequency noise peak. At each step, the fitting sinusoid is subtracted from the output signal and the process is repeated for the next dominant noise peak. This process does not need to be carried out for all the harmonic noise components but only for those frequencies that are gathered around the signal frequency. The final product is a string of data where the relevant high-amplitude components affecting the signal have been purged from the data or their peaks have been strongly reduced. The spectral analysis is then carried out on the purged data.

This technique works but it is only preliminary and other approaches will be tried in the future. The goal here is to demonstrate that a violation signal comparable to the expected threshold sensitivity can be resolved in the presence of dynamics-related noise. Another goal is to use this process to define the inertia parameters of the instrument package that lead to a successful signal extraction and avoid the saturation of the accelerometer dynamic response. Many simulations have been run to fine-tune the model and also the signal extraction process. In the following we show only a summary of cases that represent different dynamical situations and their effect on the response of the differential accelerometer.

Prograde, low-frequency precession

Results of simulations with (prograde) precession frequency substantially lower than the spin frequency ($\Omega << \nu$) are shown in Figure 8 and Figure 9. These cases are associated with a minor-axis spinner in which the precession is in the same direction of the spin (prograde precession). In the first case the precession frequency is 0.05 Hz which has a period of 20 s that covers the entire measurement time span and the spin frequency is 0.5 Hz. In the second case the precession frequency is 0.1 Hz and the spin frequency 0.5 Hz. In both cases, the signal is "masked" by the frequency peaks associated with the spin dynamics even after the signal extraction from the dynamic noise. The spin dynamics of the multi-body system generates several peaks at frequencies that are multiple of the precession frequency one of which may overlap with the signal. One possible strategy is to position those peaks in a way that the peaks do not cover the signal. In the following we will explore the option of using precession frequencies that are higher than the spin (i.e., retrograde precession) to this end.

Damped 25% for 5 s, Elastic freq. = 3 Hz; Ix = 0.3; Iy = 0.3, Iz = 0.27 (0.05 Hz prograde)
Rate error = 0.1 deg/s, Elevation angle = 0.1 deg; Spin = 0.5 Hz;
del-xA = del-yA = del-zA = 10 μm; del-xB = del-yB = del-zB = 11 μm;
Signal = 1x10^-14 g; Noise = 0 g; Initial xA = xB = 50 μm

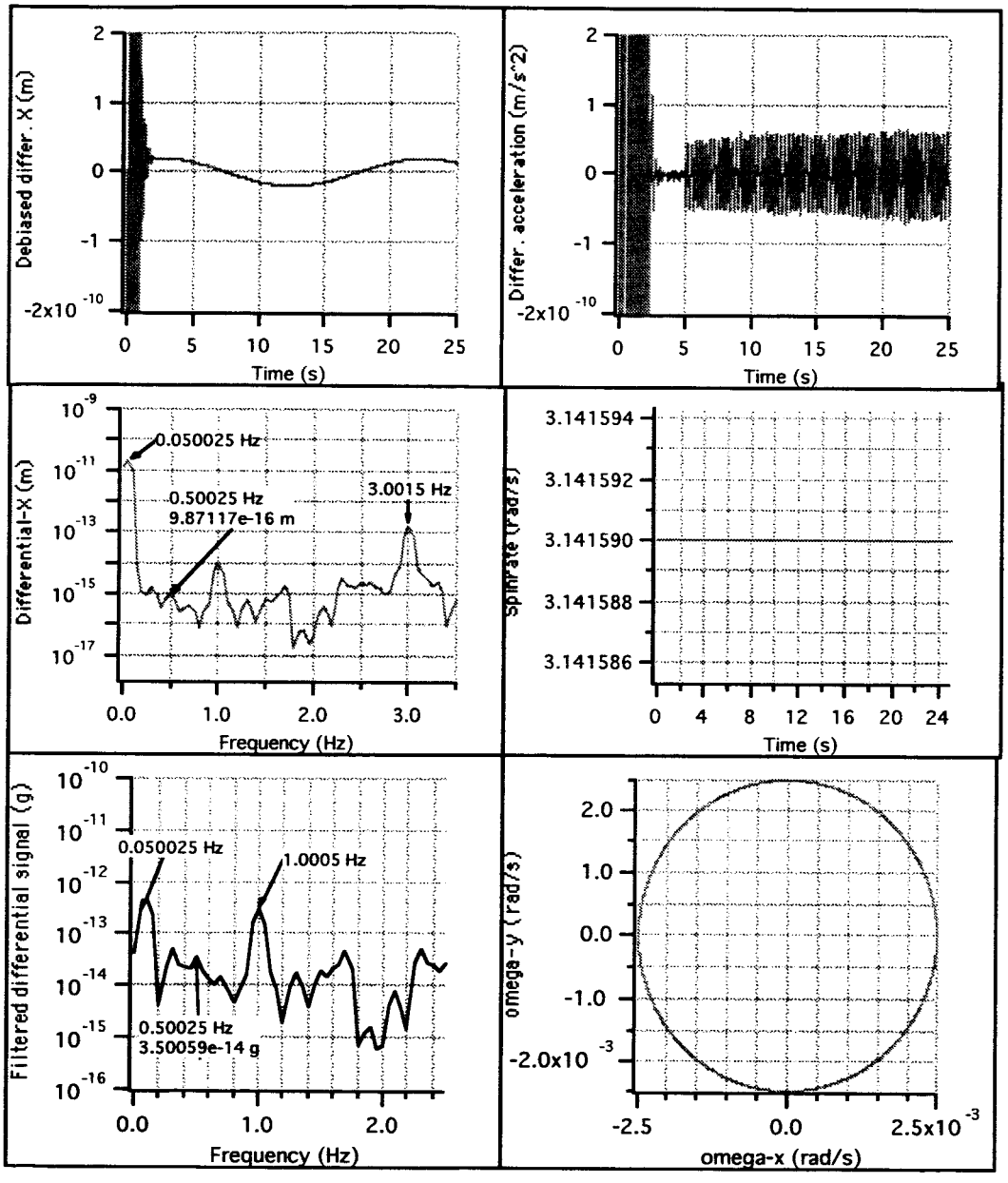

Figure 8 Dynamic response for precession = 0.05 Hz and signal = 0.5 Hz

Damped 25% for 5 s, Elastic freq. = 3 Hz; Ix = 0.3; Iy = 0.3, Iz = 0.24 (0.1 Hz prograde)
Rate error = 0.1 deg/s, Elevation angle = 0.1 deg; Spin = 0.5 Hz;
del-xA = del-yA = del-zA = 10 μm; del-xB = del-yB = del-zB = 11 μm;
Signal = 1x10^-14 g; Noise = 0 g; Initial xA = xB = 50 μm;

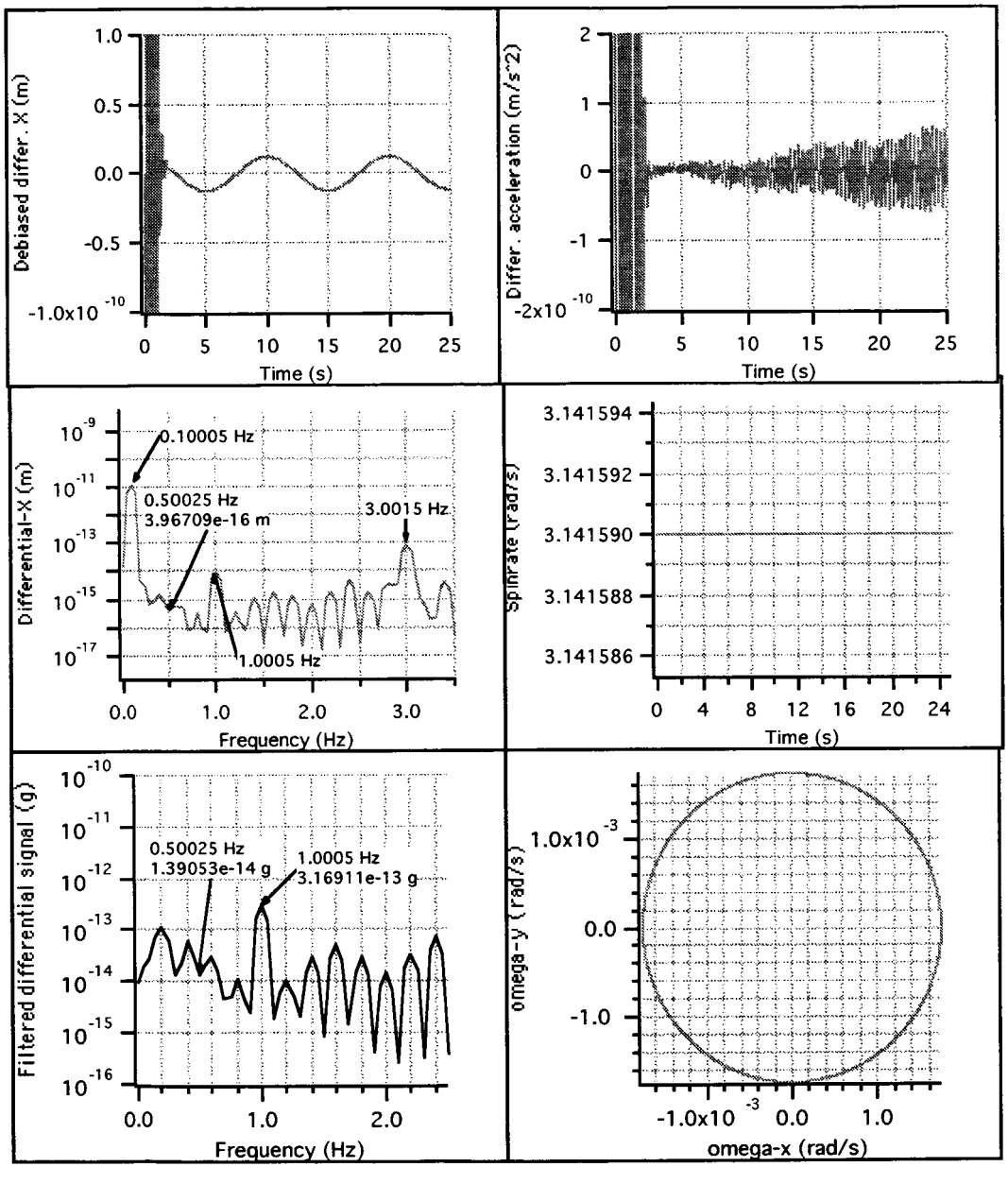

Figure 9 Dynamic response for precession = 0.1 Hz and signal = 0.5 Hz

Retrograde precession

One option that we analyzed consists in placing the body precession frequency past the spin frequency. In these cases the spinning body must be a major-axis spinner and the precession is retrograde with respect to the spin. Although this option might be appealing at first sight because all the harmonics which are multiple of the precession frequency do not interfere with the signal frequency, the drawback is the substantially strong increase in dynamics-related acceleration.

As explained earlier, the acceleration at a point off the spin axis is proportional to $(\Omega - \nu)$ and, consequently, a prograde spin increases the acceleration substantially because Ω, being negative, adds up to the spin ν. The increase can saturate an accelerometer that has to measure accelerations as low as 10^{-14} g because the dynamic range for these instruments are typically equal to 10^6 and, hence, the saturation value of the acceleration is of order 10^{-8} g.

In Figure 10 we have assumed a spin frequency equal to 0.3 Hz and a precession frequency of 0.5 Hz. The raw acceleration (unfiltered) at the precession frequency exceeds 10^{-9} g (which is near the saturation value) and this peak overshadows the signal frequency by being too close to it. A different filtering scheme than the one outlined above may yield somewhat better results but the fundamental problem with the saturation remains.

In Figure 11 the precession frequency is equal to 1 Hz and the spin frequency to 0.3 Hz. In this case the peak at the precession frequency is dangerously close to the saturation limit of the accelerometer. The signal is somewhat better resolved than in the previous case because of the larger frequency separation between the signal (with strength = 1×10^{-14} g) and the precession frequency. A better filtering scheme could further improve the recovery of the signal. However, it is not advisable to have steady acceleration components that can potentially saturate the dynamic range of the accelerometer.

Damped 25% for 5 s, Elastic freq. = 3 Hz; Ix = 0.3; Iy = 0.3, Iz = 0.8 (0.5 Hz retrograde)
Rate error = 0.1 deg/s, Elevation angle = 0.1 deg; Spin = 0.3 Hz;
del-xA = del-yA = del-zA = 10 μm; del-xB = del-yB = del-zB = 11 μm;
Signal = 1x10^-14 g; Noise = 0 g; Initial xA = xB = 50 μm

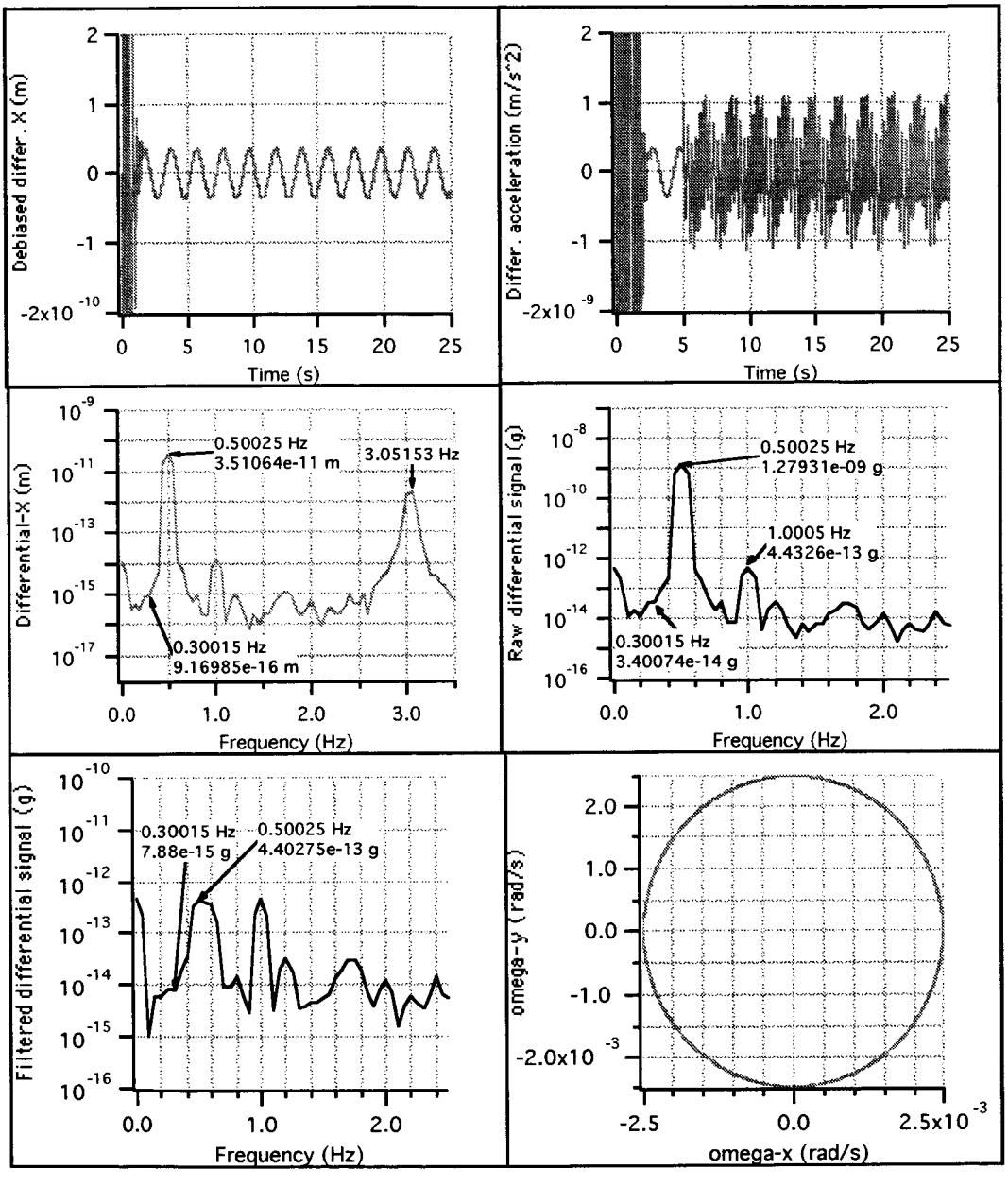

Figure 10 Dynamic response for precession = 0.5 Hz and signal = 0.3 Hz

Damped 25% for 5 s, Elastic freq. = 3 Hz; Ix = 0.3; Iy = 0.3, Iz = 1.2 (1 Hz prograde)
Rate error = 0.1 deg/s, Elevation angle = 0.1 deg; Spin = 0.3 Hz;
del-xA = del-yA = del-zA = 10 μm; del-xB = del-yB = del-zB = 11 μm;
Signal = 1x10^-14 g; Noise = 0 g; Initial xA = xB = 50 μm

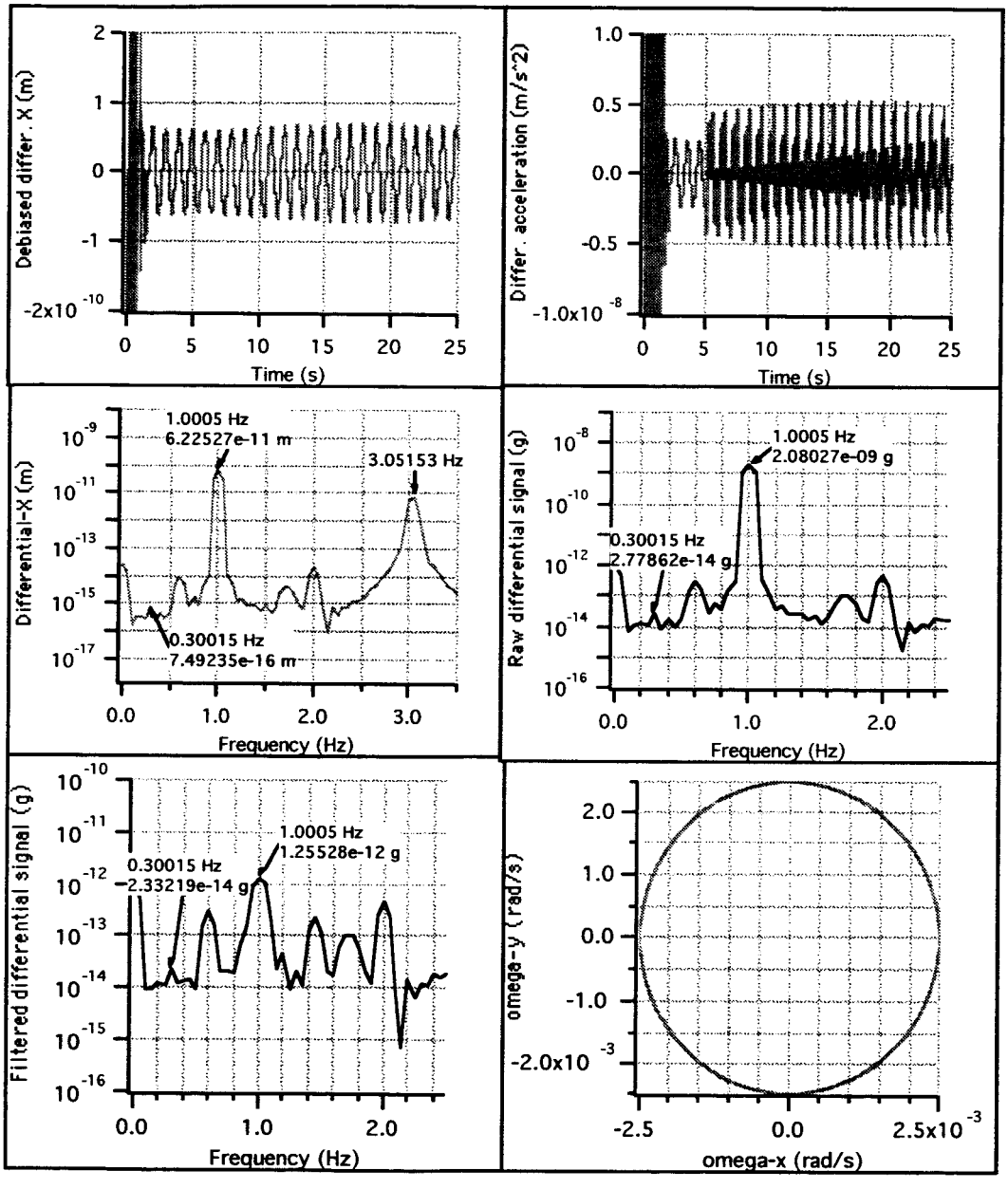

Figure 11 Dynamic response for precession = 1 Hz and signal = 0.3 Hz

Prograde, intermediate-frequency cases

The low-frequency-precession cases have issues with the precession frequency multiples interfering with the signal but otherwise the strength of the dynamics-related peaks are lower than the cases with retrograde precession. The high-frequency-precession cases have more serious issues associated with the dynamics-related harmonics being too close to the saturation value of the accelerometer. The problems afflicting the prograde precession cases could be mitigated (or solved) by choosing the precession frequency in such a way that the signal frequency falls in between two successive dynamics-related peaks.

The following figures show two cases of a minor-axis spinner in which the precession frequency has been selected according to the criterion expressed above. Figure 12 shows results for a run with precession frequency = 0.2 Hz and signal frequency = 0.5 Hz. In this case the signal peak falls in between the second and third harmonics of the precession-related frequencies. After considering that our signal extraction procedure is only preliminary, we have increased the violation acceleration (signal) strength to 2×10^{-14} g. However, we have added a white noise to the accelerometer output with an RMS acceleration-equivalent value of 4.5×10^{-14} g to represent broad-spectrum noise sources related to the detector.

Figure 13 shows results for a run with precession frequency = 0.3 Hz and signal frequency = 0.5 Hz. In this case the signal peak falls in between the first and second harmonics of the precession-related frequencies. We have also added the same violation signal and the white noise as in the previous case.

In both cases the signal can be extracted successfully. From inspection of the results, it appears that the former case (precession = 0.2 Hz) led to a better recovery of the signal than in the latter case. However, it is premature to make a strong distinction between the two cases because the recovery of the signal depends on the details of the extraction process which, as stated previously, is preliminary. Both cases appear acceptable.

As a more general conclusion, we can state that a minor-axis spinner is preferable than a major-axis spinner. Moreover, the precession frequency should be reasonably close to the signal frequency and chosen in such a way that its multiples do not overlap directly with the signal frequency.

The results shown here indicate that a small violation acceleration at the spin frequency can be extracted from the much higher dynamics-related noise. The analysis also provides essential guidelines on how to choose the moments of inertia of the instrument package. A preliminary technique for extracting the signal from a broad-banded white noise and specific dynamics-related harmonics with much greater amplitude has also been implemented. The analysis can be carried further into several directions as follows:

a) Specialize the model to reflect the geometry of the suspension system of the proof masses of the differential accelerometer as the design of the flight instrument matures;

b) Analyze the sensitivity to asymmetries in the transverse moments of inertia of the package and mass differences between the proof masses.

c) Explore alternative techniques for extracting the signal from noise.

Damped 25% for 5 s, Elastic freq. = 3 Hz; Ix = 0.3; Iy = 0.3, Iz = 0.18 (0.2 Hz prograde)
Rate error = 0.1 deg/s, Elevation angle = 0.1 deg; Spin = 0.5 Hz;
del-xA = del-yA = del-zA = 10 μm; del-xB = del-yB = del-zB = 11 μm;
Signal = 2x10^-14 g; Noise = 4.5x10^-14 g; Initial xA = xB = 50 μm

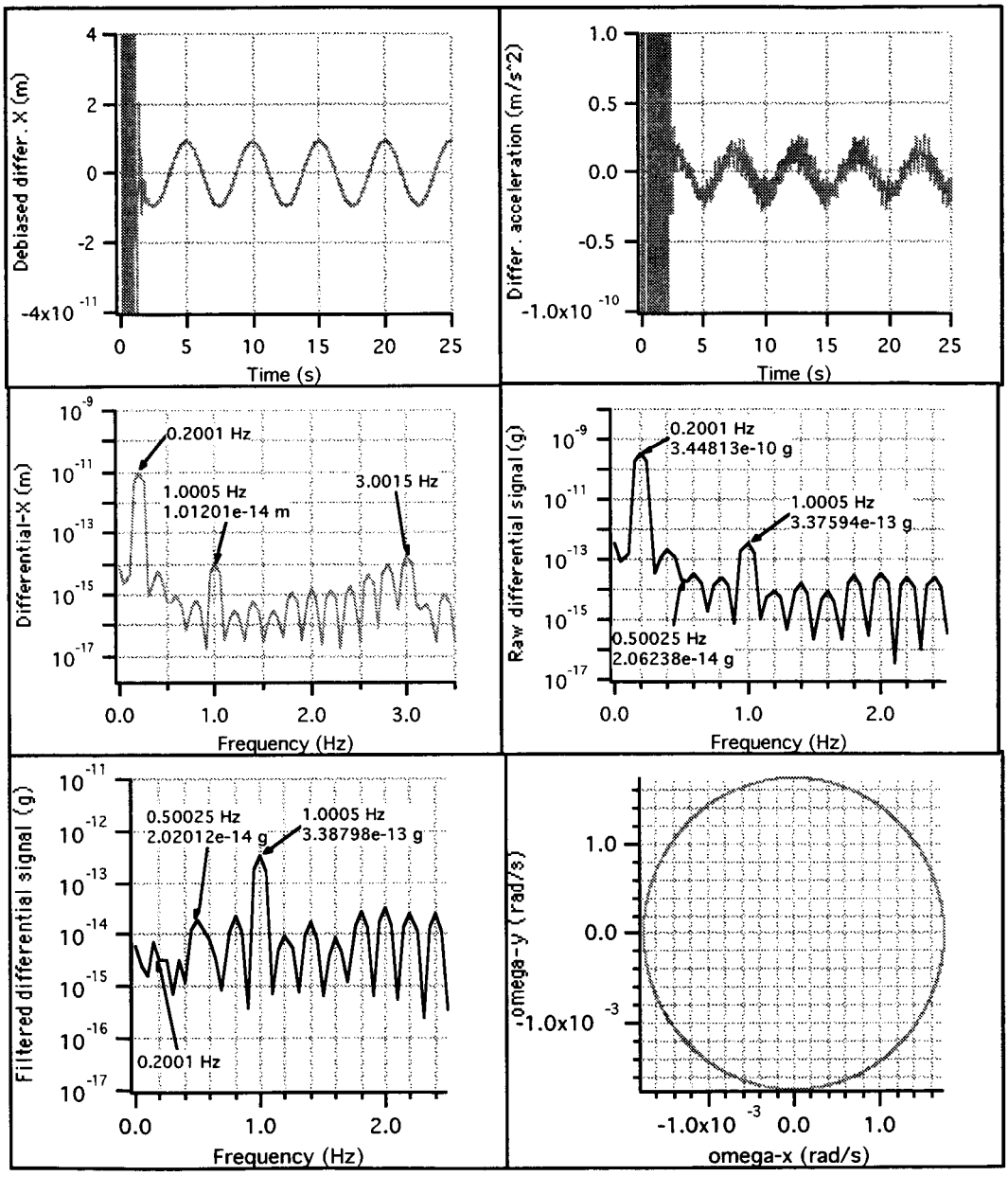

Figure 12 Dynamic response for precession = 0.2 Hz and signal = 0.5 Hz

Damped 25% for 5 s, Elastic freq. = 3 Hz; Ix = 0.3; Iy = 0.3, Iz = 0.12 (0.3 Hz prograde)
Rate error = 0.1 deg/s, Elevation angle = 0.1 deg; Spin = 0.5 Hz;
del-xA = del-yA = del-zA = 10 μm; del-xB = del-yB = del-zB = 11 μm;
Signal = 2x10^-14 g; Noise = 4.5x10^-14 g; Initial xA = xB = 50 μm

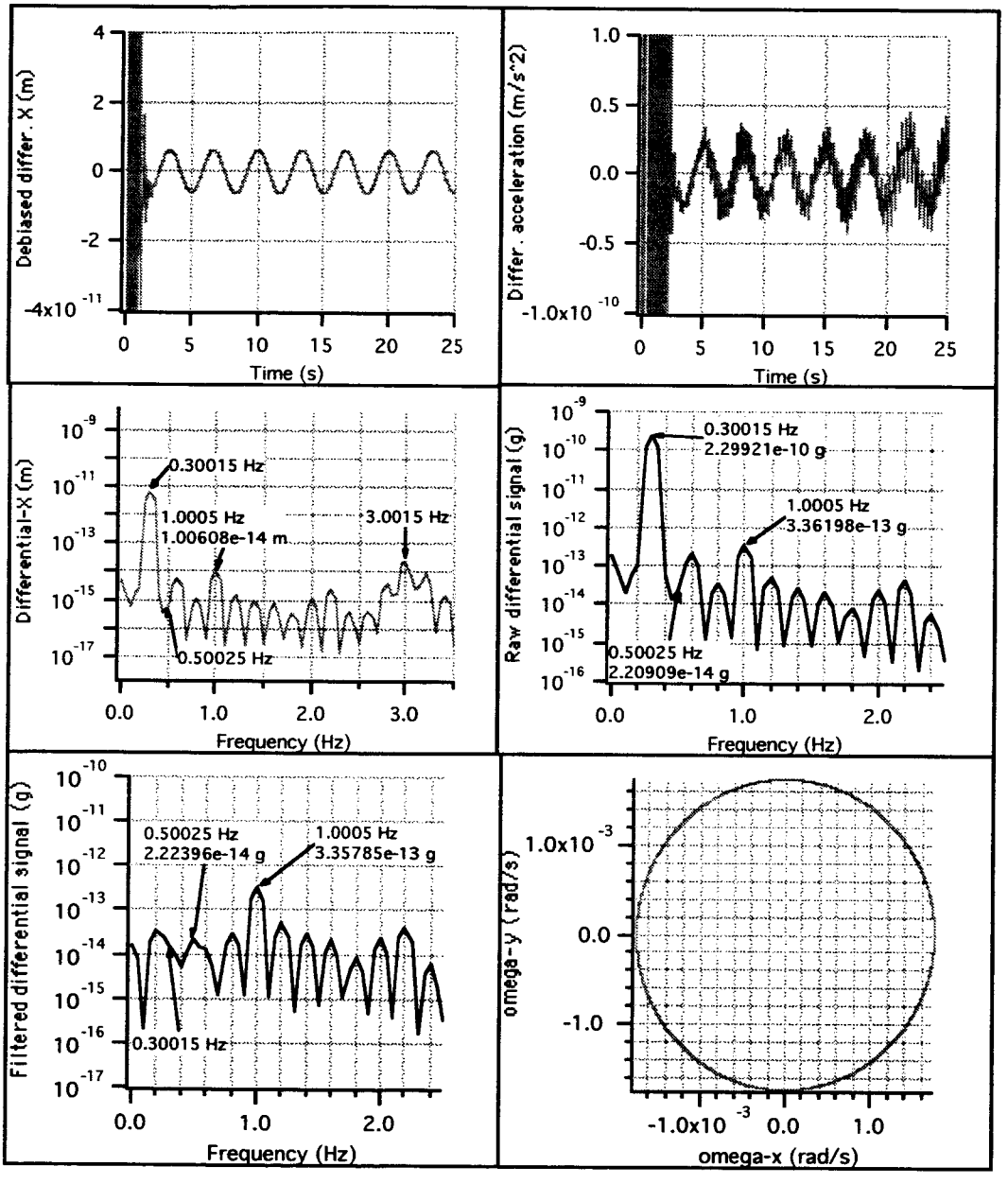

Figure 13 Dynamic response for precession = 0.3 Hz and signal = 0.5 Hz

Mechanical Design

Balloon/Capsule Dynamic model

Introduction

The balloon-shroud-gondola-capsule system is an articulated mechanical system which is subjected to environmental perturbations as it raises to altitude that will make it oscillate. The capsule must be released well within 0.1 deg from the local vertical in order to meet the requirements placed on the orientation of the differential accelerometer with respect to the horizontal plane during the fall.

The capsule orientation must be controlled by acting on its attachment point to the gondola in order to keep the capsule as aligned as possible with the local vertical in spite of the oscillations of the upper part of the oscillating system. We call the system that accomplishes this control the leveling mechanism. First we assume that the gondola (as in several balloon flights) maintains its pointing (to the North for example) through its own control system. Then the leveling mechanism will have to control the two angles that defines the orientation of the longitudinal axis of the capsule with respect to the local vertical.

The dynamics model that we adopt follows these assumptions. We analyzed in details the control about one axis as the other one has similar features. Two options are investigated: in option 1 the control is exercised by torqueing the capsule with respect to the gondola; in option 2 the attachment point of the capsule to the gondola is adjusted by moving it laterally. The model, control strategies and results for the two options are discussed in the following.

Model description

The model is a 6 DoF pendulum system composed of balloon, shroud, gondola and capsule. The balloon center of mass (CM) is modeled as 'attached' to the nominal altitude (40 km) with a spring in order to simulate buoyancy-induced oscillations typical of stratospheric balloons. These oscillations have low frequencies (periods of 200 s to 300 s) and vertical amplitudes of about 300 m.

Wind acts on the balloon only (the high ballistic coefficients of capsule and gondola make their combined contribution negligible).

Before attempting a design of the leveling system, initial conditions for the pendulum motion in the worse case scenario must be assumed. For this purpose we performed an extensive literature examination including processed flight data from previous stratospheric balloon missions and scientific articles related to stratospheric balloons.

One important fact to be kept in mind is that high altitude wind conditions vary significantly according to the season, the wind speed around the winter and summer solstices being considerably higher than around the spring and fall equinoxes (seasonal wind reversals).

Quoting the "Scientific Ballooning Handbook" (see Ref. [iii]): "Characteristically, at float, the amplitude of the pendulous motion is of the order of a few minute of arc, with one degree representing a reasonable design limit"

Data from the MAXIMA Experiment pre-flight test show a peak pendulum motion amplitude of 20 minute of arc at float. Data from the MSAM Experiment flight tests show a peak amplitude of 10 minute of arc at float. Following these considerations we assume 1 deg as a control design limit.

As the balloon altitude changes, the wind shear causes the balloon to accelerate and decelerate while the suspended train, whose ballistic coefficient is a factor of a thousand smaller than the one of the balloon, remain virtually unaffected by the wind velocity change. All of this induces a low frequency pendulum motion in the system which couples together with the other pendulum modes.

At stratospheric altitude the maximum value for the wind shear is 40m/s per km altitude (Ref. [ii]) under worst-case conditions away from the Spring and Fall wind reversals.

SYSTEM PARAMETERS

- Balloon radius: R = 66 m;
- Shroud length (balloon train): L = 70 m;
- Shroud moment of inertia: Is = 30000 kgm^2;
- Distance gondola CM (C_3 in Figure 14) from shroud-gondola attachment point: r = 2.7 m;
- Distance gondola CM from capsule-gondola attachment point: h =2.7 m;
- Distance capsule CM from capsule-gondola attachment point: d = 2.8 m;
- Gondola width: R_gon = 3 m;
- Total capsule vertical length: h_cap = 5.6 m;
- Capsule radius: R_cap = 0.7 m;
- Mass of gondola: m_G = 300 kg;
- Mass of capsule: m_C = 1000 kg;
- Mass of balloon (including He) + attached mass:
  m_{att} = 2400 kg;
  m_b = 1530 kg;
- Moment of inertia of balloon (inner gas not counted): I_b = 2584092 kgm^2;

- Moment of inertia of gondola about CM:
$I_g = 1/12*(m_G)*(h+r)^2+1/4*(m_G)*R\_gon^2$;

- Moment of inertia of capsule about CM:
$I_c = 1/12*(m_C)*h\_cap^2+1/4*(m_C)*R\_cap^2$;

- Oscillation amplitude: $A\_osc = 300$ m;

- Balloon cross section: $A_d = 14000$ m^2;

- Air density at 40 km of altitude: $\rho\_air = 3.851 \times 10^{-3}$ kg/m^3;

- Balloon drag coeff: $C_d = 0.5$;

LEVELING CONTROL RATIONALE

When no control is applied the capsule is acted upon by a torque from the gondola attachment point which causes it to oscillate.

In order to prevent the capsule from oscillating we considered four possible solutions:

1) Counteract the torque by torqueing the capsule against the gondola.

2) Actuate a relative motion between capsule and gondola in order to align the force at the rigging-gondola attachment point with the overall center of mass of the gondola plus the capsule.

3) Counteract the torque externally (e.g. using jets)

4) Counteract the torque internally (with reaction wheels)

Option 3 is considered too complex whereas option 4 poses significant problems of reaction wheel desaturation. Options 1 and 2 have been examined in more details and are described in the following.

CONTROL OPTION 1: Torque motors on the capsule-gondola joint

The first solution examined exploits a torque motor between the capsule and the gondola (Figure 14) which allows the alignment of the center of mass of the gondola-capsule assembly with the force transmitted at the gondola-rigging attachment point.

A Matlab Simulink linear time invariant model for the system including a control algorithm was developed (Figure 15). The system is able to control verticality at 0.01 deg with a simple PID feedback control.

The only issue is the amount of torque required to counteract the gravitational torque on the capsule-gondola joint. This can be on the order of 400 Nm excluding friction.

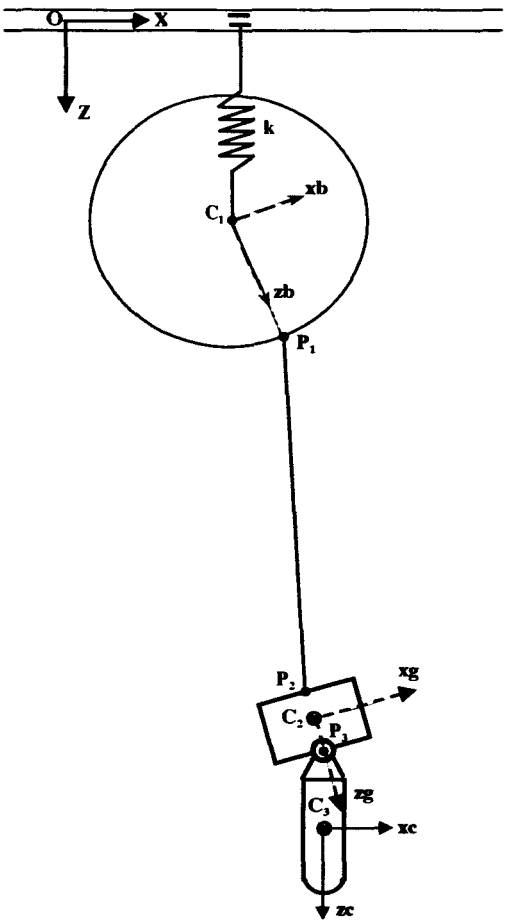

Figure 14 System schematic for option 1

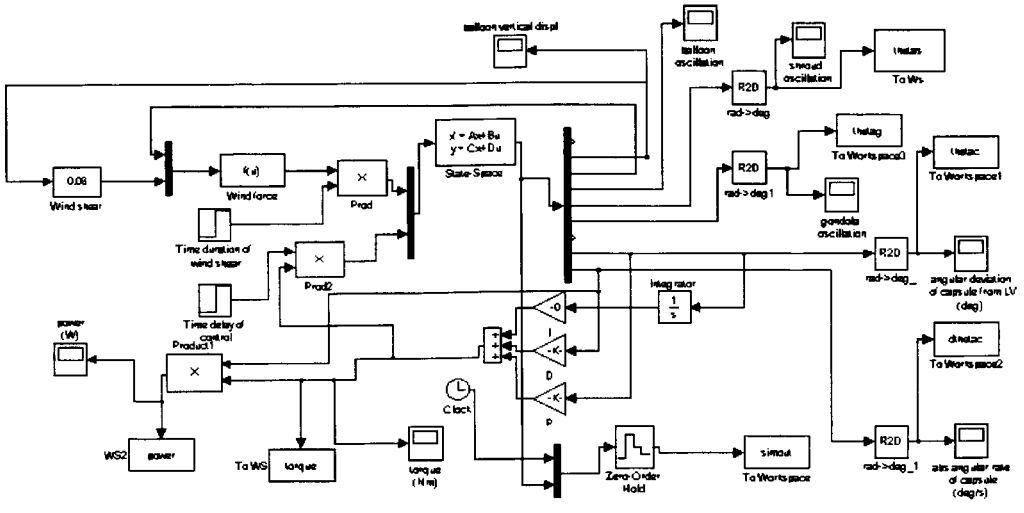

Figure 15 Block diagram of Matlab Simulink for Option 1

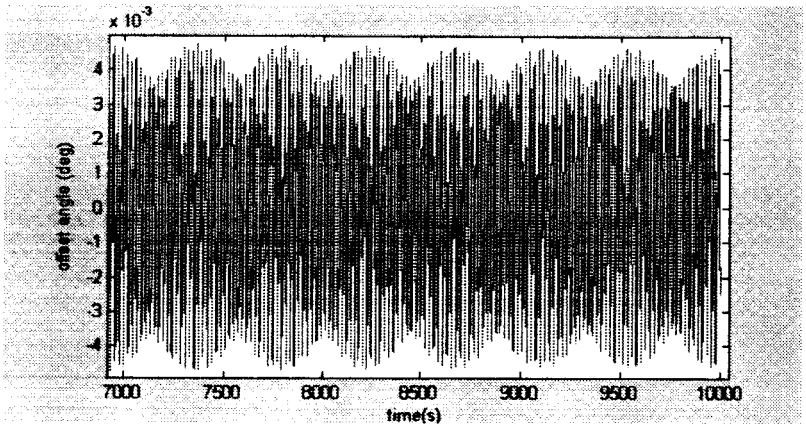

Figure 16 Capsule angular offset from local vertical

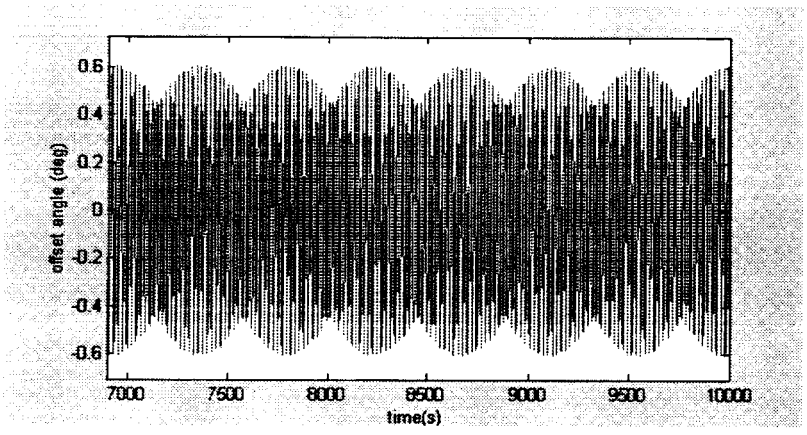

Figure 17 Shroud angular offset from local vertical

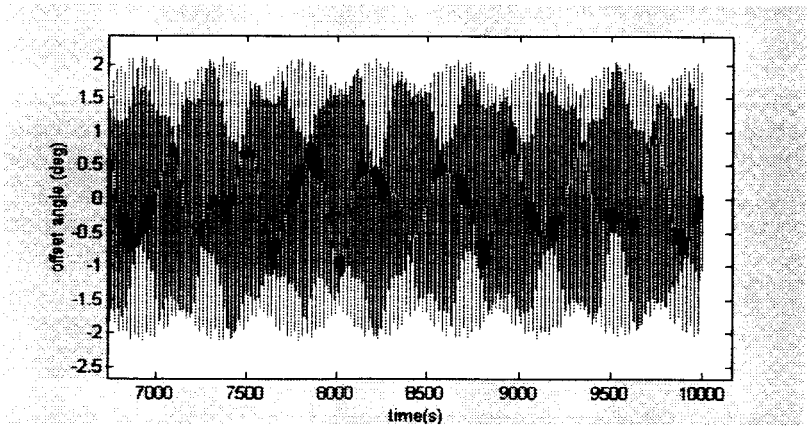

Figure 18 Gondola angular offset from local vertical

CONTROL OPTION 2: Linear motors acting on the capsule-gondola joint

The second solution examined utilizes a linear actuator between the capsule and the gondola (Figure 19) as an alternative mean to align the center of mass of the gondola-capsule assembly with the force transmitted at the gondola-rigging attachment point.

In this case the actuator does not have to counteract gravity which is a significant advantage for the proposed algorithm.

Again the dynamics of the system was studied with the aid of a Matlab Simulink linear time invariant model (Figure 20). The system performance is similar to the previous case with verticality controllable to better than 0.01 dg.

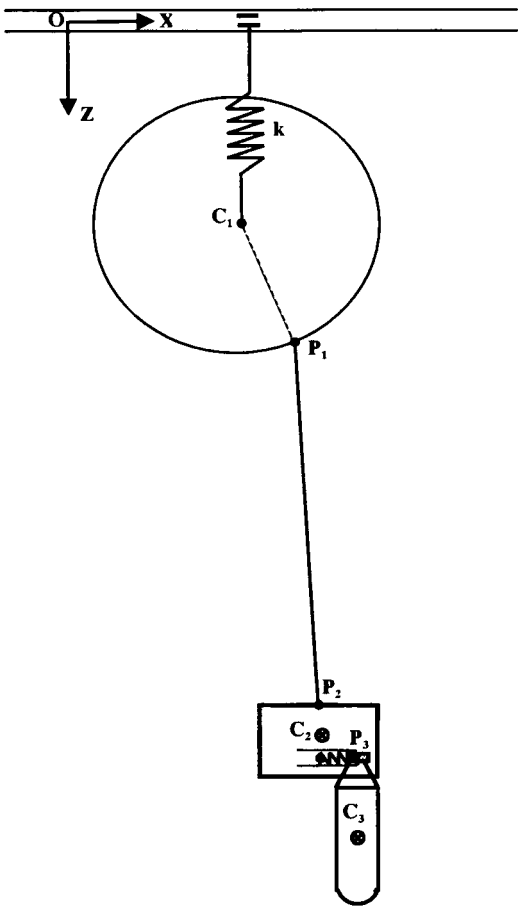

Figure 19 System schematic for option 2

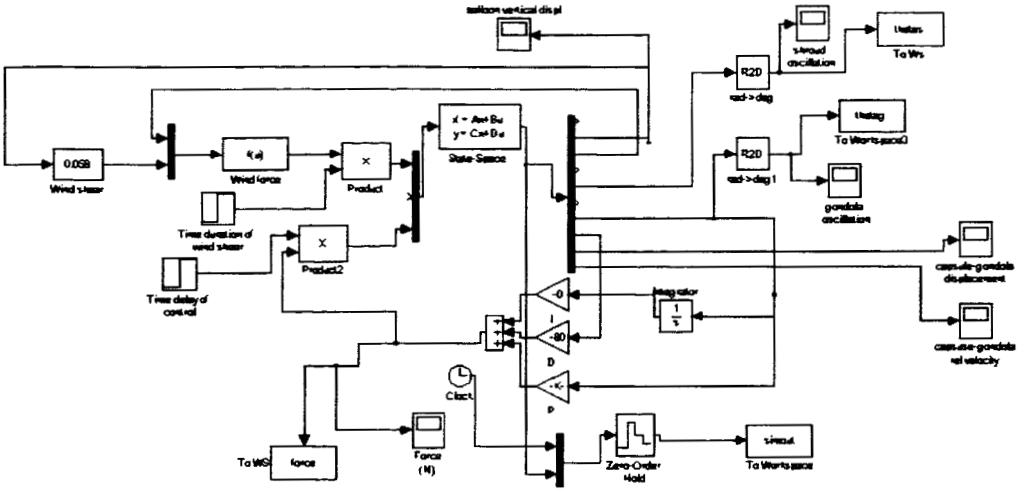

Figure 20 Block diagram of Matlab Simulink for Option 2

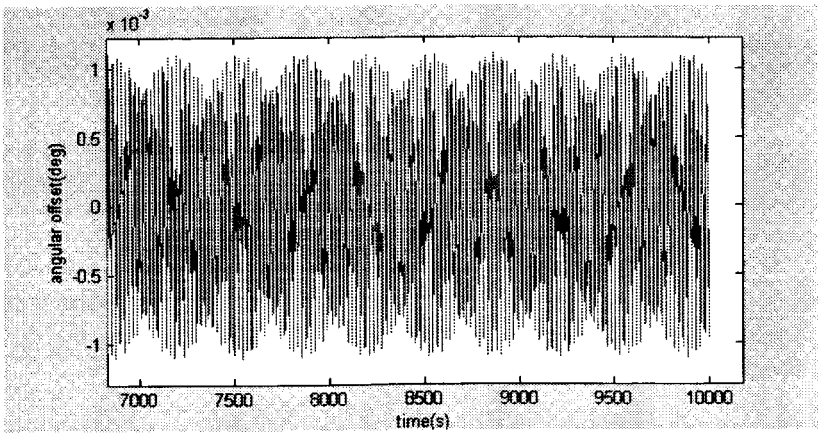

Figure 21 Capsule angular offset from local vertical

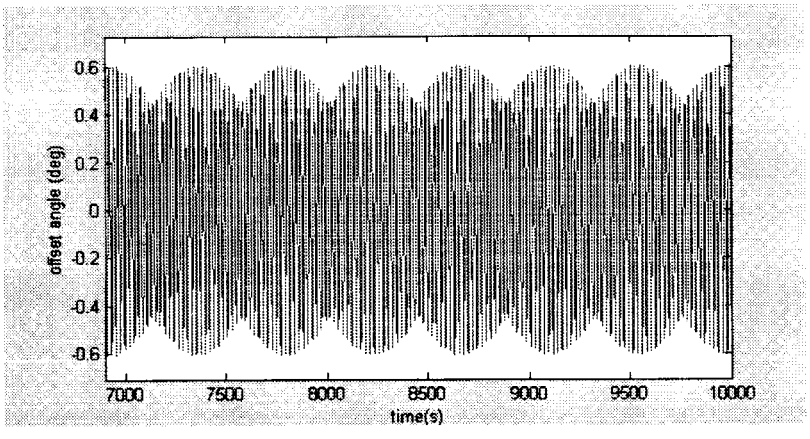

Figure 22 Shroud angular offset from local vertical

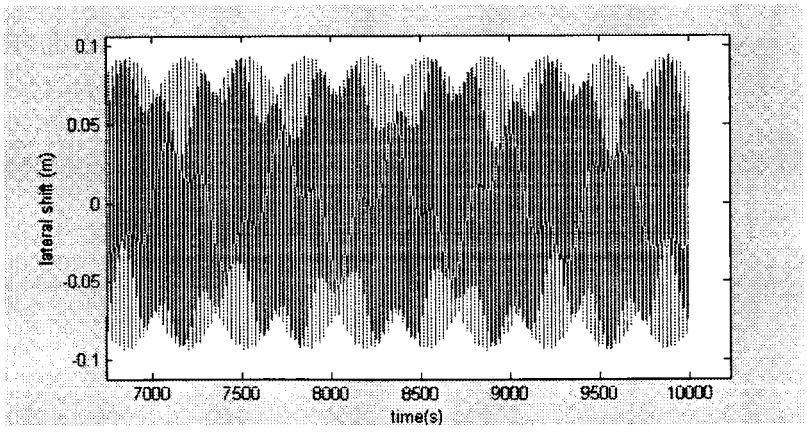

Figure 23 Capsule-gondola relative lateral displacement

Leveling mechanism

Introduction

The dynamic analysis of the balloon and capsule indicates that either mechanical option (explored in the previous section) can control the capsule verticality. However, the first option (which control the verticality by controlling the angle between the capsule and the gondola) requires high torques. In the second option, the position (on the x-y plane) of the capsule attachment point to the gondola is controlled. This option exploits better the effect of gravity on the capsule and requires relatively small lateral forces for the control. Consequently, option 2 has been adopted as the baseline for a preliminary design of the leveling mechanism which is described in the following.

Mechanical description

The x – y translator assembly consists of two linear translation mechanisms and their support structures positioned orthogonally to each other and a payload support structure mounted to linear motion blocks (LM blocks) on the upper translator assembly (see Figure 24). The payload release mechanism, with rigid hub and flange, passes through two large square openings in the lower and upper translator assemblies and bolt to the underside of the payload support structure (see Figure 25). There is ample clearance to allow +/- 16.5 cm (+/- 6.5 in.) travel of the payload hub and interface flange (the maximum travel can easily be increased).

The two translator assemblies, are identical except that the lower assembly drives the upper assembly and the payload in the y-y direction. The lower assembly bolts to the gondola structure. The upper translator assembly drives the payload support structure and the payload in the x–x direction. The upper translator assembly is mounted to LM Blocks on the lower translator assembly.

Each translator assembly (see specifications) consists of a rectangular box beam structure, rail support plate, two LM guide rails with four blocks, electric thrust cylinder fitted with spherical rod end, motor brake and clevis pinned to the rod end and attached to the structure above it.

Weight (Total, x–y Translator assembly): 347 kg (764 lb)
(does not include interface flanges, hub and release mechanism)

Mechanism Specifications

ELECTRICAL THRUST CYLINDER (2 REQ'D):

- IDC MODEL NO. EC5-B41-100-32B (WITH SPHERICAL ROD-END AND MOTOR BRAKE)
- 10 / 1 GEARS, 32 mm / REV BALLSCREW

- MAX SPEED: 89 mm / s (3.5 in. / s)
- MAX THRUST @ 100 % DUTY CYCLE : 635 kg (1400 lb.)
- ESTIMATED THRUST TO MOVE PAYLOAD: 23 – 91 kgm (50–200 lb.)
- LINEAR STROKE: +/- 16.5 mm (+/- 6.5 in.)
- REPEATABILITY: +/- 0.013 mm (+/- .0005 in.)
- LEAD ACCURACY: +/- 0.05 mm / 30cm (+/- .002 in./ft.)
- MOTOR: RARE EARTH BRUSHLESS SERVO WITH
  2000 LINE ENCODER AND COMMUTATION SENSORS
  POWER (PEAK) : 885 WATTS
  POWER (100 % DUTY CYCLE CONTINUOUS) : 427 W
- WEIGHT : 29 kg (57 LB.)

LINEAR MOTION GUIDE RAIL AND LM BLOCK (4 RAILS AND 8 LM BLOCKS REQ'D):

- THK MODEL NO. HSR30LA–M OR HSR30-LB-M
- 4-ROW CIRCULAR ARC CONTACT DESIGN WITH RECIRCULATING BALLS. CAN BE PRELOADED.
- DYNAMIC LOAD RATING: 37.3 KN (8,393 LB.)
- STATIC LOAD RATING: 62.5 KN 914,062 LB.)
- MATERIALS (BLOCKS, RAILS AND BALLS) : STAINLESS STEEL
- RAILS MAY BE CUT TO NON – STANDARD LENGTHS
- LENGTH OF RAILS : 1.35 M (4.42 FT.)
- RUNNING PARALLELISM : LESS THAN .01 mm (.0004 IN.)
- WEIGHT (TOTAL, RAILS AND BLOCKS): 36 kg (80 LB.)

BOX BEAM STUCTURE (2 REQ'D) :

- MATERIAL : 6 IN. X 4 IN. RECTANGULAR STEEL TUBING (MODULAR CONSTRUCTION CAN BE RESIZED AT LOW COST.
- WEIGHT (EACH) : 100kg (220 LB.)

RAIL SUPPORT PLATE (2 REQ'D):

- MATERIAL : ALUMINUM PLATE WITH LOCALLY MACHINED FLATS AND PERPENDICULAR EDGES TO POSITION THE GUIDE RAILS PARALLEL AND COPLANAR
- WEIGHT (EACH) : 16 kg (35 LB.)

PAYLOAD SUPPORT STRUCTURE:

- MATERIAL : WELDED CONSTRUCTION ALUMINUM PLATE
- WEIGHT : 45 kg (100 LB)

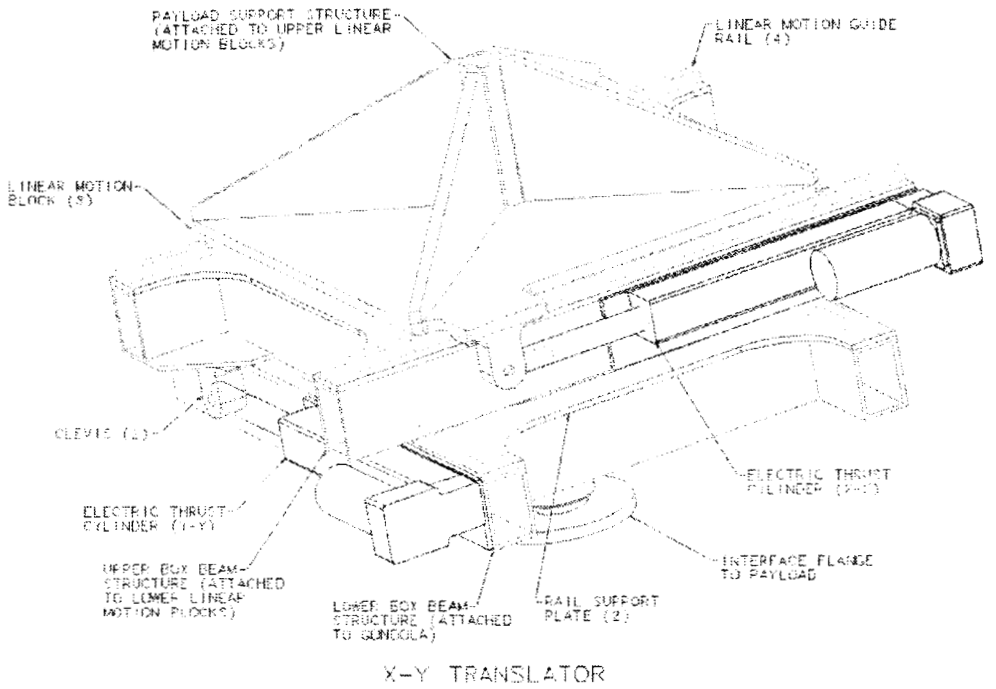

Figure 24 Upper view (from the gondola side) of the leveling mechanism

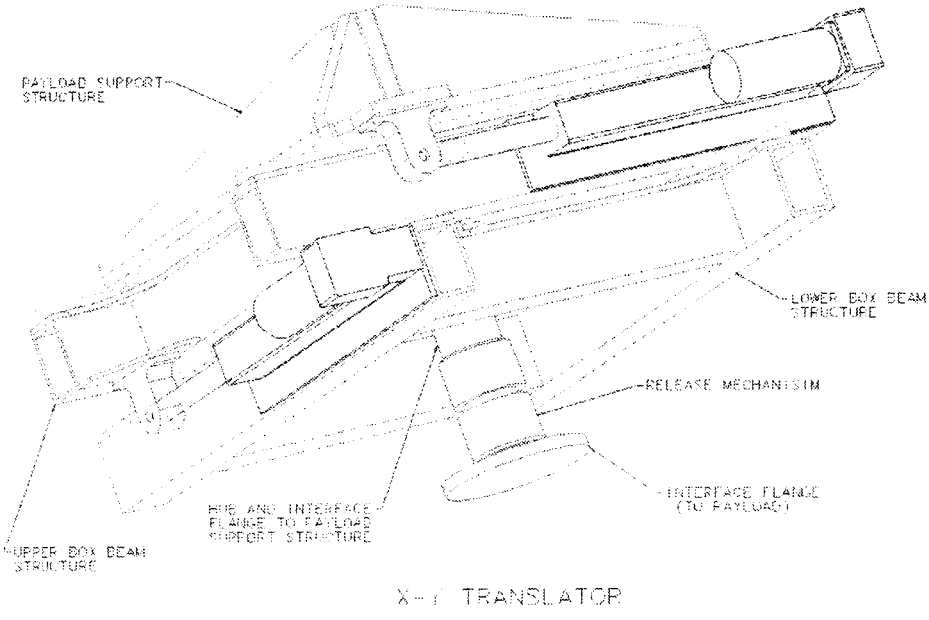

Figure 25 Lower view (from the capsule side) of the leveling mechanism

Thermal Analysis of Instrument Package

Introduction

The new conceptual design of the cryostat (see next section) calls for a dewar that is mostly at the LHe temperature (we assumed 5K at the walls to account for heat leakages) except for one end of the cryostat (the access door) which is at the LN2 temperature. We need to answer the question: how is the temperature distribution in the sensor (i.e., differential accelerometer) going to be affected by the non-symmetric temperature distribution in the cryostat? Will the sensor still meet the requirement placed on spatial temperature gradients smaller than 0.2 deg/m? These issues are analyzed in the following subsections in which the temperature distribution throughout the sensor is computed after letting it seat (without rotating in this analysis) for 10000 s inside the cryostat and then switching on the preamplifier for 2000 s. The first time interval is close to the expected duration of the ascent phase of the balloon, while the second time interval is representative of the check out phase before experiment release.

Assumptions

(1) At the start, the entire experiment except the electronics (not shown in the figure) start at 5K. The dewar is also at 5K except for one end, which is 1m in diameter, about 0.5m (a conservative value) from the experiment, and set to 77K (LN2 temperature).

(2) The sensor is protected from direct radiation from the electronics and preamp with shields as before.

(3) The preamp is off until the last 2000 sec. in this model (i.e. from 0 to 10000 sec).

(4) Linear conductors represent the shaft and wiring from electronics -> preamp -> sensor. The wires are modeled as Constantan.

(5) The experiment is not rotating, which provides conservative estimates for the spatial thermal gradients.

Results:

The majority of experiment heating is still conductively coupled from the electronics, which raises the experiment temperature from 5K to about 5.5K for the gold-plated experiment shell (see Figure 26). If the experiment is "black" (emittance 0.93), there is a small amount of additional warming - over the 12000 sec the final temperature reaches 5.82K (see Figure 27).

In both cases, the gradients in the shell of the experiment are very small (less than 0.015K/m in the worst case, which is shown in Figure 28). In the first case (gold), the gradient is entirely axial for the cylinder. As can be seen in this last figure, the "black" experiment shows a small amount of asymmetry due to the 77K surface (toward the top

in this view). In both cases the spatial temperature gradients (K/m) and the temperature drifts (K/s) of the sensor are comfortably within the requirements. [see Ref. [iv]].

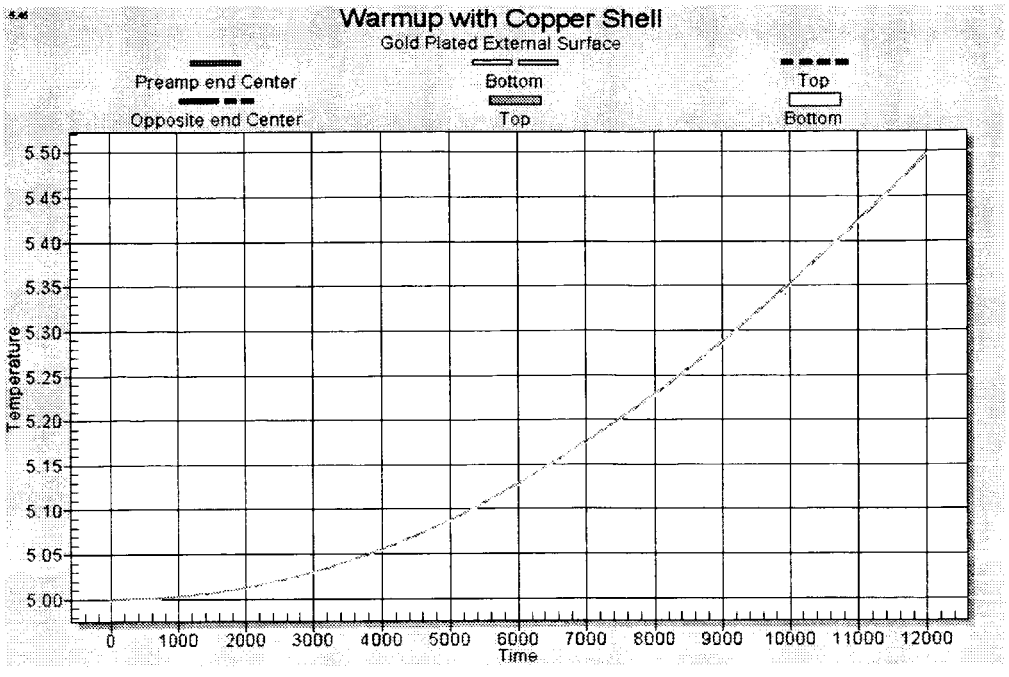

Figure 26 Warm-up with Gold-plated Copper shell: temperature (K) vs. time (s)

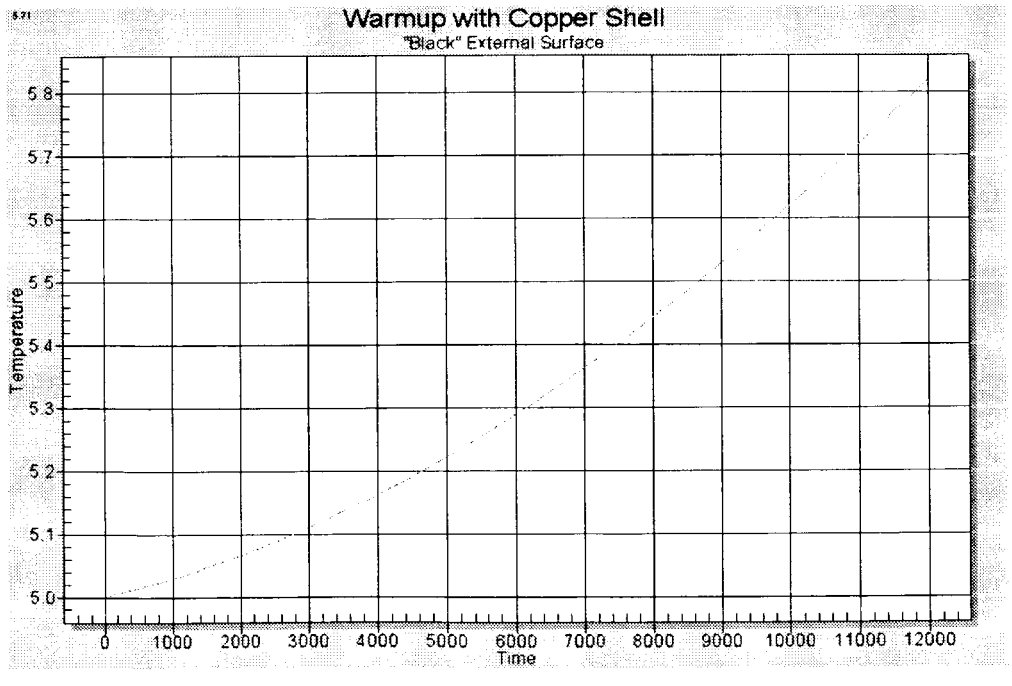

Figure 27 Warm-up with black-coated Copper shell: temperature (K) vs. time (s)

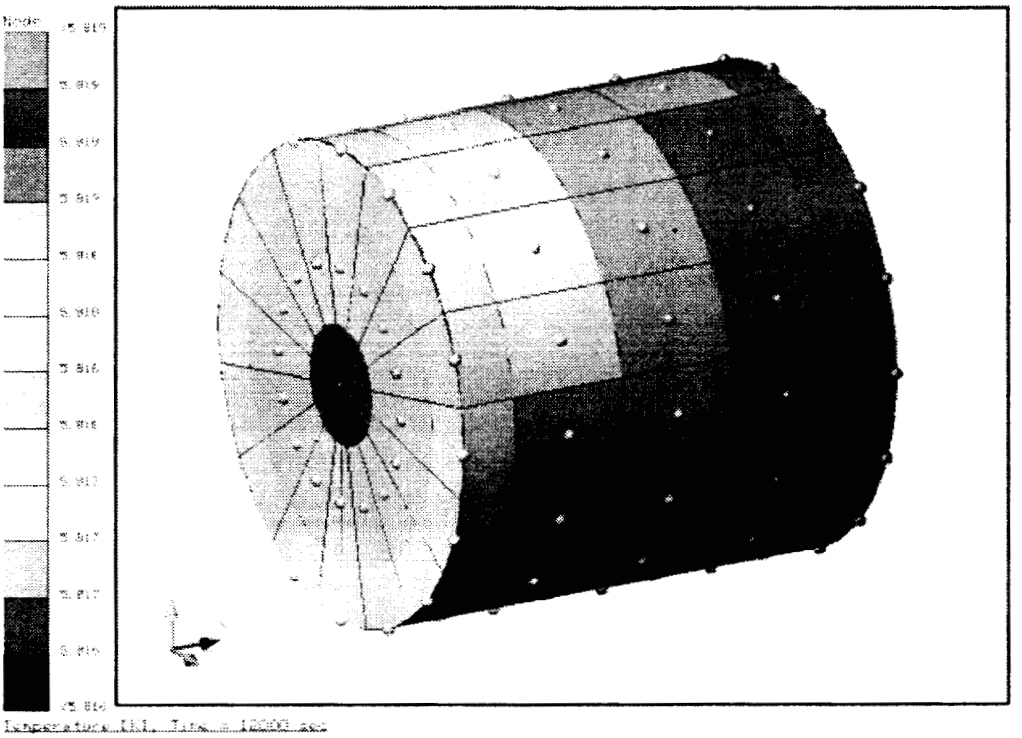

Figure 28 Temperature distribution (K) in sensor after 12000 s

Design Activity at IFSI on New Instrument Prototype*

Introduction

The design of a new instrument prototype has been worked out at the Institute of Space Physics (IFSI). The new instrument prototype design improves several characteristics of the previous instrument prototype by increasing the rejection of common-mode acceleration and the response to rotational velocities and accelerations. In the new prototype design the two masses are pivoted on the same side. This arrangement leads to the rejection of both common-mode acceleration and rotational velocities and accelerations. The prototype proof masses are shaped like hollow cylinders which are simpler to build than the teethed cylinders described previously. Hollow cylinders can also be sized in a way to minimize the higher-order mass moments (in particular the quadrupole term), although, the two proof masses need to have different lengths in this case. This constraint is not met by the new prototype which is aiming for easiness of construction. Mitigation of the higher-order mass moments are not necessary in a laboratory prototype that can not be tested down to the level of those gravity perturbations.

Another important change in the new design are the mechanical suspensions of the proof masses which are made with flat flexures as opposed to squared torsional springs. The flexures provides a much better separation between the 'sensitive' frequency and all the other elastic frequencies of the accelerometer. As a result, the accelerometer exhibits a much lower cross-talk sensitivity to perturbations which are not aligned with the sensitive axis.

Another important change is that the capacitive pickups of the new prototype are now along the cylinder's surfaces and no longer at their bases. Hollow cylinders do not have a large base and, consequently, it is better to use the larger (outer or inner) cylindrical surfaces for attaining the desired electro-mechanical coupling (that is the desired ratio between mechanical energy of the proof masses and electrical energy stored in the capacitive pickups).

Figure 29 is a schematic cutout of the prototype differential accelerometer that shows the two proof masses (in yellow and blue), their flexural suspensions, and the capacitive pickups (in red). The accelerometer can be assembled and disassembled along the axial direction. It practically consists of four concentric cylindrical elements (two of which are the proof masses) held together by the top and bottom plates (in grey).

The flexural suspensions and proof masses are designed in such a way as to have an natural frequency of the differential mode of a few Hz (that can be lowered by electrostatic feedback) when the accelerometer operates vertically with the proof masses hanging as indicated in Figure 29.

* Section contributed by our non-US partners at IFSI/CNR

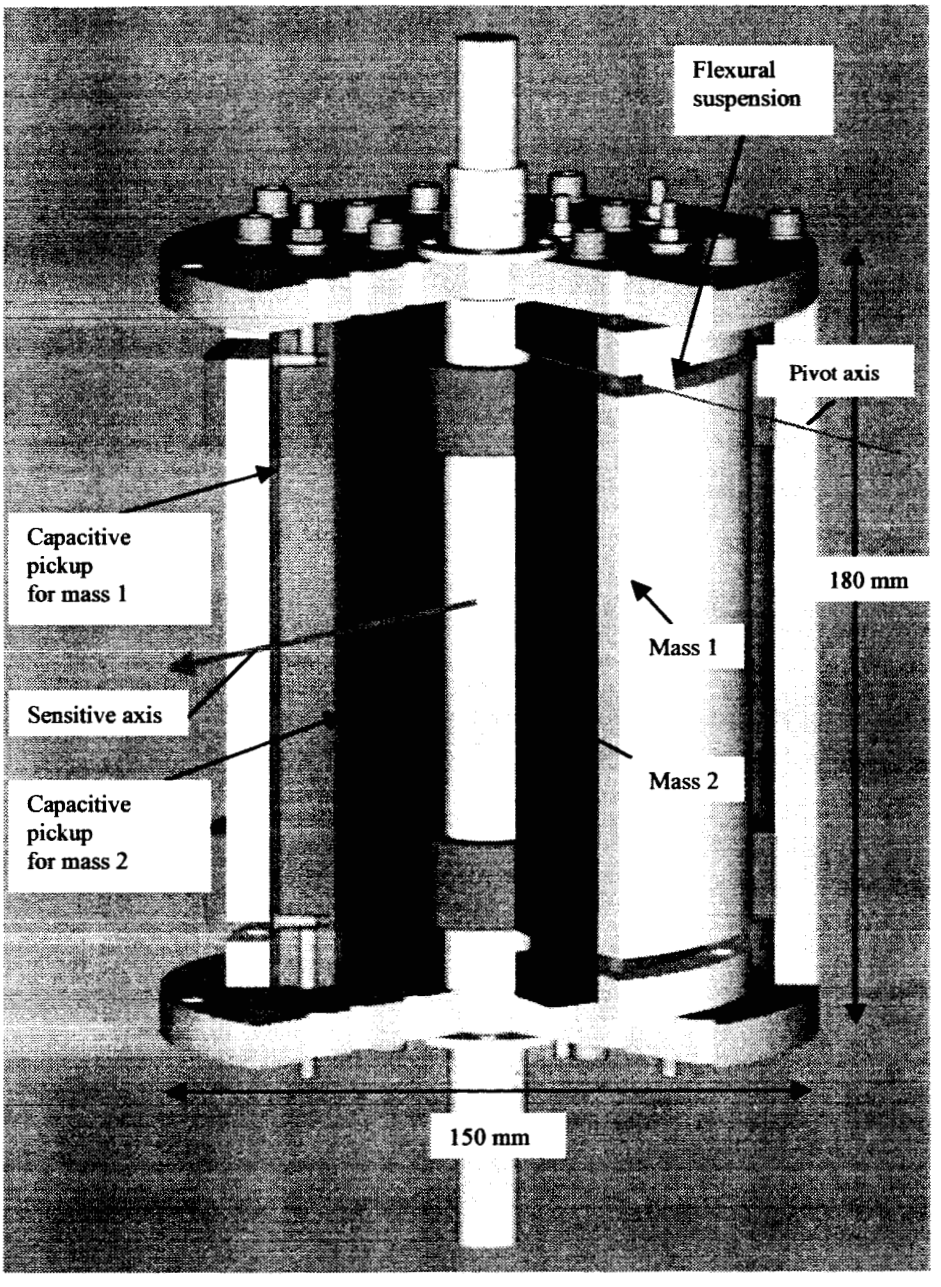

Figure 29 Cutout view of the new differential accelerometer prototype

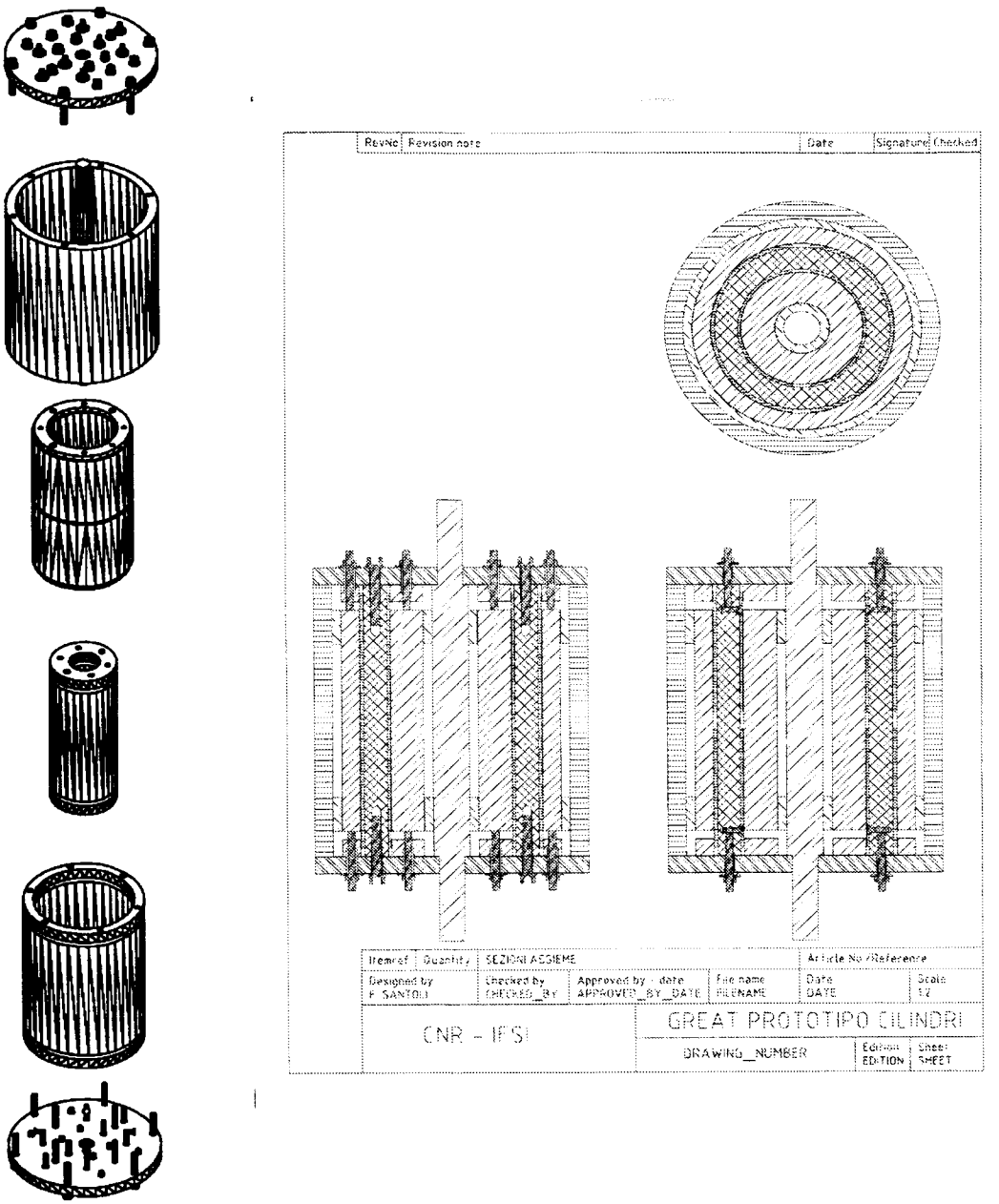

Figure 30 Differential accelerometer prototype assembly

Dimensioning of flexural suspensions

The team at IFSI utilized a finite-element-model (FEM) to analyze the modal frequencies of a mass (of rectangular cross section in this model) as a function of the characteristics of the flexural suspension. The goal is to compute the separation among the first few natural frequencies. The suspended mass in this case has dimensions 56 x 63 x 34 mm, the flexural suspension has a surface of 56 x 5 mm and a thickness of either 190 μm or 200 μm. The material for both the suspended mass and the flexure is aluminum with a density of 2700 kg/m^3. Two values of the Young modulus were adopted as follows: 63 GPa or 73.1 GPa. The attachment of the flexure to the wall was also assumed either as rotationally and translationally fixed (into a wall) or through the interposition of a aluminum frame anchored at its sides as shown in Figure 31.

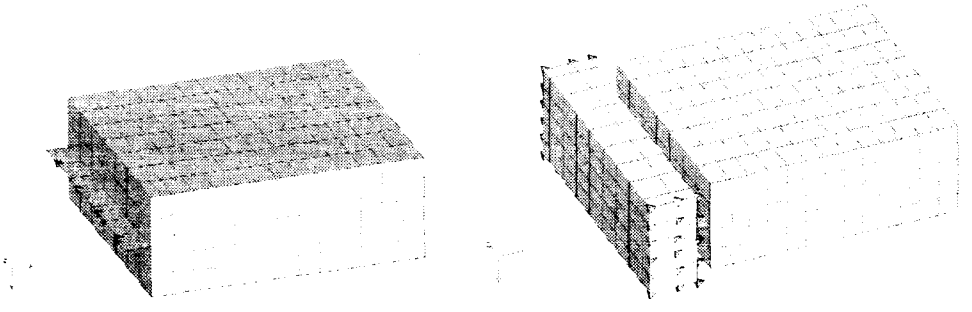

(a) (b)

Figure 31 Details of the suspension attachment: (a) fixed and (b) framed

A summary of the configuration analyzed and their characteristics is shown in Table 1. Four modal shapes associated with the first four natural frequencies are shown in Figure 32 through Figure 35 for configuration No. 5 of Table 1.

Table 1 Characteristics of flexural suspensions analyzed

Configuration number	Flexure thickness (μm)	Young modulus (GPa)	Type of constraint	Finite element type	Number of elements	First frequency (Hz)
1	200	73.1	Fixed	Solids	623	6.92
2	200	69	Fixed	Solids	623	6.70
3	190	73.1	Fixed	Solids	623	6.40
4	190	69	Fixed	Solids	623	6.21
5	190	73.1	Framed	Solids	731	6.38
6	190	69	Framed	Solids	731	6.19

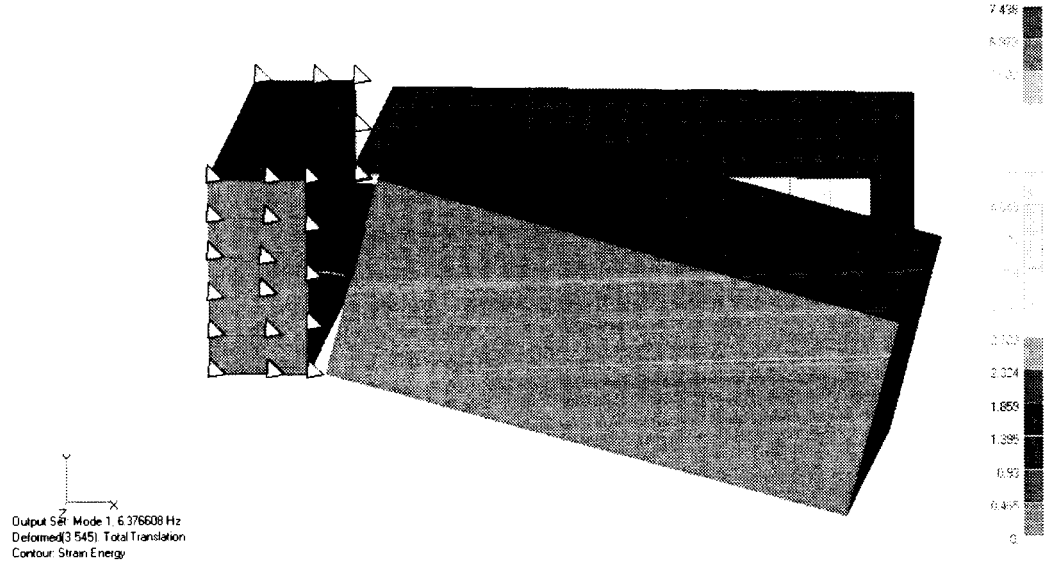

Figure 32 First mode (pure bending)

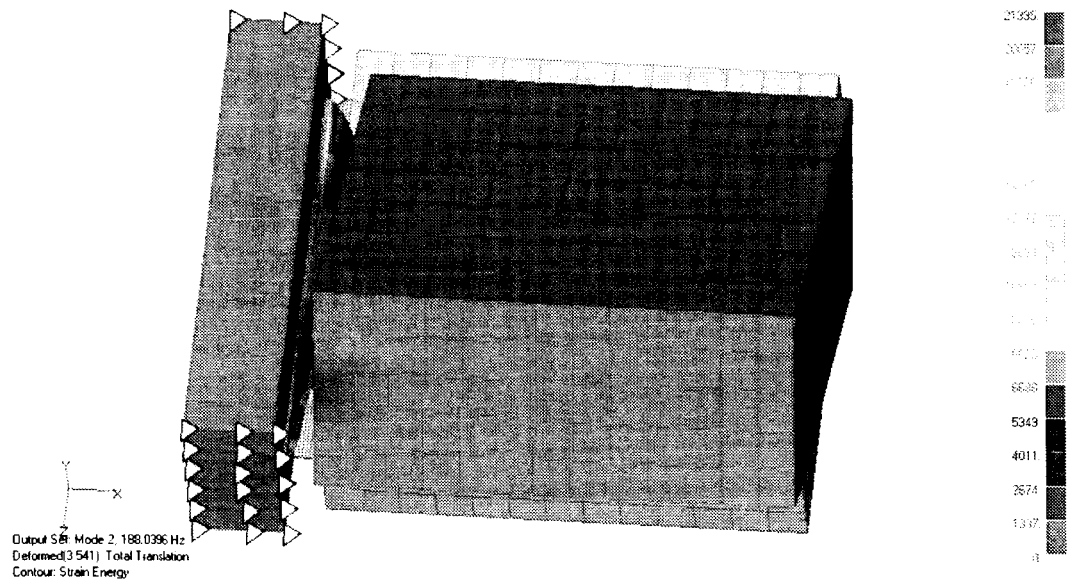

Figure 33 Second mode (torsion)

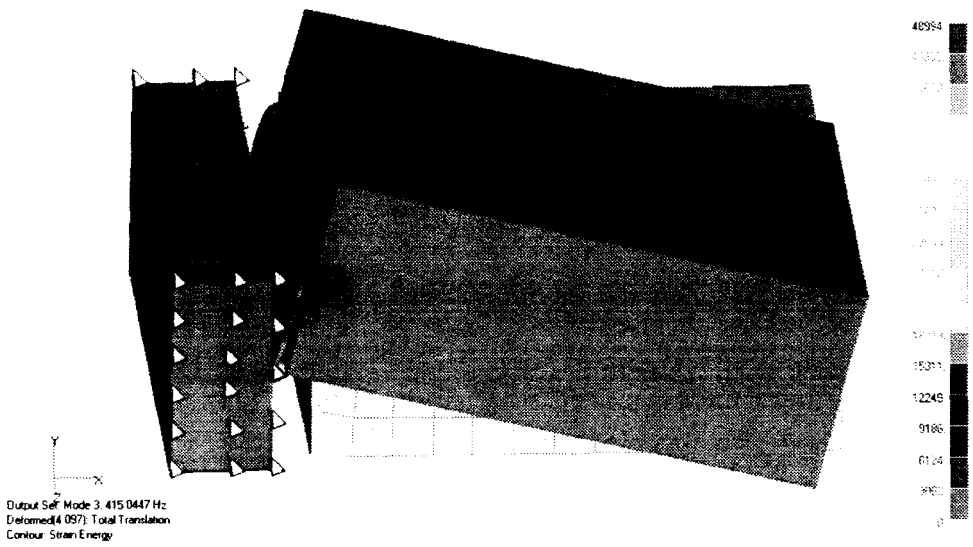

Figure 34 Third mode (double bending)

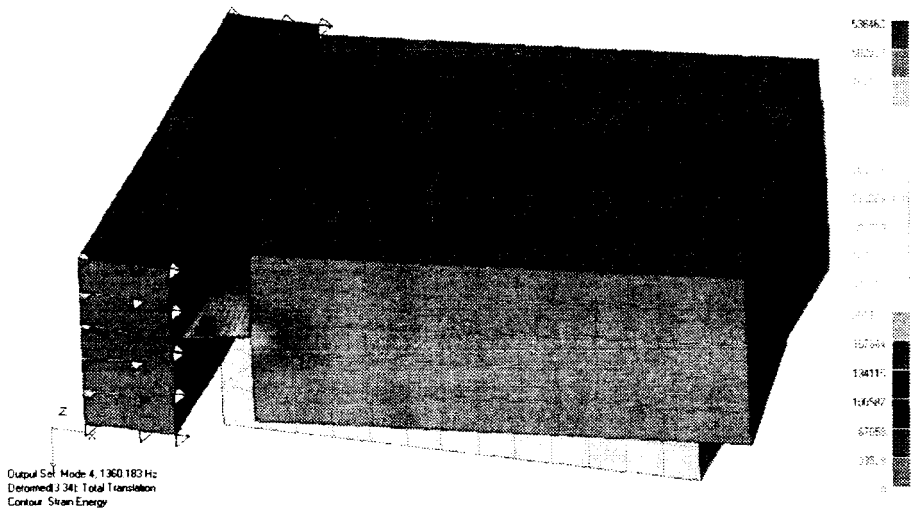

Figure 35 Fourth mode (side bending)

The first four natural frequencies for all the configurations of Table 1 are shown in Table 2. The key point is that the first (bending) frequency is conveniently low, at about 6-7 Hz, while the other natural frequencies are high and well separated from the first frequency. Consequently, the accelerometer responds 'softly' to an acceleration along its sensitive axis while it is insensitive to acceleration along an axis that is not aligned with the sensitive axis.

Table 2 Natural frequencies

Configuration number	1st frequency (Hz)	2nd frequency (Hz)	3rd frequency (Hz)	4th frequency (Hz)
1	6.92	205.21	453.36	1452.68
2	6.70	198.65	438.86	1406.20
3	6.40	190.15	420.11	1412.59
4	6.21	184.74	408.16	1372.41
5	6.38	188.04	415.04	1360.18
6	6.19	182.69	403.24	1321.49

The frequencies quoted above are in the absence of a gravity field. For testing on ground, the proof masses will be subjected to a 1-g field and the natural frequencies will change depending on whether the accelerometer is upside up or upside down. In the former case the proof masses are suspended at the top like a regular pendulum while in the latter case they are suspended from the bottom like an inverted pendulum.

The first oscillation frequency f_1^g, in the presence of the 1-g field, can be computed from the 'free" frequency f_1 as follows:

$$f_1^g = \sqrt{f_1^2 \pm \frac{Mgd}{4\pi^2 I_z}}$$

where M is the mass of the proof mass, g the Earth's gravity acceleration, d the distance between the proof mass CM and the pivot axis and I_z the moment of inertia with respect to that axis. The plus sign applies to the regular pendulum and the minus to the inverted pendulum.

For the values adopted for this study with d = 34 mm, M = 0.23 kg and $I_z = 3.5 \times 10^{-4}$ kg/m^2, the first-mode frequency without gravity, for the up and down positions of the accelerometer are shown in Table 3.

Table 3 First frequency with and without gravity field

Configuration number	First frequency No gravity (Hz)	First frequency Regular pendulum (Hz)	First frequency Inverted pendulum (Hz)
1	6.92	7.31	6.51
2	6.70	7.10	6.27
3	6.40	6.82	5.95
4	6.21	6.64	5.75
5	6.38	6.80	5.93
6	6.19	6.62	5.73

The results of the finite element analysis have been used to size the flexures of the new instrument prototype.

Preliminary Design of Customized Cryostat

Topsfied Engineering Services (TES) was recommended by the cryostat manufacturer Janis Research Company (Wilmington, MA) for carrying out the preliminary design of a large, customized cryostat. We have asked TES to provide us with a phase-I preliminary design of the cryostat to be incorporated into the free-fall capsule. We specified an experimental (internal) cylindrical volume of at least 1m diameter x 2m height; a maximum mass of less than 500 kg; an internal pressure lower than 10^{-9} torr; easy and wide access to the inside of the cryostat for mounting the experimental equipment; a temperature during the free fall phase at the sensor below 10 K (with a desire to reach lower values); the ability to vent all the refrigerants before experiment drop; and the ability to maintain temperature after cool down and experiment launch for 5 hours.

As a result of the thermal analysis carried out previously, we had determined that a cryostat with a colder area (LHe) and a warmer end (LN2) was acceptable from the thermal point of view. This design would simplify the opening and closing of the cryostat (from the bottom) because the LHe dewar becomes one unit without any access door and interruption of feeding lines. This solution was proposed to Topsfield Engineering as the starting point of their preliminary design.

Also we determined that there are electrical motors (for the spin up system) commercially available which are capable of operating at the LHe temperature and, consequently, the LHe dewar does not need to be interrupted with enclosures, at higher temperature, to accommodate the motors.

The first report from Topsfield Engineering is shown in Appendix A.

Appendix A – Report from Topsfield Engineering (TES)

Topsfield Engineering Service, Inc.
PO Box 436
Hingham, MA 02043

Smithsonian Astrophysical Observatory
1815 Massachusetts Avenue
Cambridge, MA 02138
ATTN: Peter N. Cheimets

DATE: 6 February 2004
FROM: Paul-W. Young/William Bell
PHN: 781-740-1015
MEMO: 03373-1

CC: None

SUBJECT:

References

SAO Statement of Work DTD 10/14/2003

Overview

This report develops the concept for providing a Dewar System that will be capable of providing an experiment volume that is at a temperature of <10 K and a vacuum of < 10^{-9} Torr for a period of up to eight hours during, pre-launch, launch, and the experiment phases of the experiment. This Dewar will be capable of supporting an instrument package of about 30 Kg weight within the inner vessel, and withstand the requirements of balloon lifted to altitudes of 40 Kilometers. The Dewar Assembly shall be capable of withstanding a release at altitude and a cushioned landing without damage.

It is intended to describe a Dewar System Design approach and to identify areas where there are technical risks.

Dewar System Design

The Dewar System described within this report incorporates as much of the original requirements as possible while modifying others, where required, to generate a feasible design that will meet the essential requirements for the Experiment.

The Dewar System encompasses the hardware subsystems and a procedure for setup, startup, and operation during pre-launch, launch, release & experiment, reentry, and landing. The procedures drive the design of the hardware within the restraints of the Design Criteria.

The following documentation is required to detail the Dewar System Design:

1. Top Level System Specification
2. Subsystem Specifications
3. Drawings
    a. System PFD's
    b. System P&ID – Cool down and Launch and Experiment operation
    c. Subsystem P&IDs
    d. Dewar Assembly
    e. Transport Support Assembly
    f. Utilities Skid Assemblies
    g. Electrical & Instrumentation Schematics and details
    h. Fabrication Details for Dewar, Transport Support, and Utilities Skids

Design Criteria Categories

The design criteria may be sorted into the following categories:

1. Experiment Instrument Hardware – the design responsibility is SAO's
2. Experiment Instrument support and release – the design responsibility is SAO's
3. Experiment Instrument support interface – joint responsibility SAO/TES
4. Experiment Instrument Environment
5. Experiment Instrument Operation
6. Experiment Instrument Recovery
7. Surrounding Dewar support Structure & Balloon – the design responsibility is SAO's
8. Dewar Structural
9. Dewar External Support interface – joint responsibility SAO/TES
10. Electrical and Instrumentation

This report will focus on criteria within categories 3, 4, 6, and 8. The focus will also be on 5 to the extent that the experiment instrument operation will impose requirements on the experiment instrument environment.

Hardware Subsystems

The Dewar system consists of the following hardware subsystems:

1. **Dewar Assembly**
   - a. **Upper Section**
     - 1) Outer Vessel inc/supports, piping, and electrical/inst connections.
     - 2) LN_2 Shield
     - 3) Inner Vessel & LHe reservoir
   - b. **Lower Section**
     - 1) Outer Vessel inc/supports, piping, and electrical/inst connections.
     - 2) LN_2 Shield
     - 3) Inner Vessel
   - c. **Support**
   - d. **Other Insulation**
2. **Transport Support**
3. **Cryogen Storage/Supply**
4. **Vacuum Pump (s)**
5. **External Piping**
6. **Controls & Instrumentation**

Procedures

The following procedures are developed to identify a feasible operational approach and to identify risks:

1. **Setup**
2. **Startup**
3. **Operation**

Design Criteria

The following criteria are developed and risks are identified:

Experiment Instrument Support Interface

1. Loading due to launching and balloon carry
2. Loading due to re-entry and landing
3. Experiment Instrument package weighs 30 kg
4. G level(s)
5. Positioning Accuracy
6. Effect of temperature on support assembly.
7. Support Heat Leak
8. Cabling – Instrument & Electrical

Experiment Instrument Environment

1. Vacuum < 10^{-9} torr
2. Experiment Instrument package cooled to < 10 K < 5 days.
3. Temperature of surfaces around Experiment Instrument< 10 K
4. Hold temperature and vacuum for 3 to 5 hours without external cryogen supply - from pre-launch, liftoff through free fall.
5. Minimal to no cryogen slosh that would perturb "on axis" free fall

Experiment Instrument Operation

1. Power Consumption during launch and rise to altitude.
2. Power Consumption during free fall – power source.

Experiment Instrument Recovery

1. Instrument package settles on the base of the inner vessel and can withstand reentry, parachute deployment, and landing.

Surrounding Dewar Support Structure & Balloon

1. Dewar support release within $1/10^{th}$ degree of the local gravitational vertical.
2. Simultaneous release without imposing any moments or forces normal to the vertical axis.
3. Insulating vacuum within annular space between inner and outer vessel ~ 10^{-4} torr

Dewar Structural

1. Capable of withstanding 10g pulse or impact in any direction.
2. Outer vessel designed for full vacuum.
3. Inner vessel designed for 15 psia internal and 0 psia external.
4. Inner vessel supports to withstand load in 1. above.
5. Inner vessel capable of withstanding crash down and the loading imposed by loose .instrument package within inner vessel.
6. Dewar assembly to be balanced within tbd about vertical axis.
7. Dewar assembly weight distribution within tbd along vertical axis for aerodynamic stability.

Dewar External Support interface

1. Protrusions minimized and must be symmetrical.

Electrical & Instrumentation

1. Operation outdoors.
2. Interconnections to Experiment Instrument package to minimize heat leak.

Procedure Description

These procedures describe actions relative to the Dewar System.

Setup

1. All components of the Dewar Assembly and associated cryogen and vacuum piping will have been tested for leakage prior to acceptance and use
2. MLI shall be applied to subsections of Dewar, as required, prior to assembly.
3. Dewar Assembly is accomplished in a clean room environment
4. All support equipment, Cryogen Storage/Supply, Vacuum pumps, interconnecting piping and instrumentation, and power shall be skid mounted and portable. All connections shall be protected for transport to the launch site.
5. The Experiment Instrument package is assembled into the upper section of the Dewar Assembly by attaching it to the support points within the inner vessel.
6. Connect and test out all Experiment Instrument package instrument and electrical feed throughs.
7. Assemble inner vessel lower section and leak test
8. Assemble LN2 shield and leak test
9. Assemble outer vessel and leak test during evacuation, backfill with He, and evacuation x times to assure that all condensable gas is removed
10. Perform evacuation and backfill with Gn2 on LN2 shield to assure that all condensable gas is removed prior to filling with LN2
11. Perform evacuation and backfill with He x times to assure that all condensable gas is removed from Inner vessel and Experiment Instrument package
12. Pump down insulating vacuum to tbd and verify that rate of rise is < tbd
13. Transport the Dewar Assembly to the Launch site

Startup – at Launch Site

1. Fill Dewar LN2 reservoir with LN2 to cooldown inner vessel to 80 K.
2. Inner vessel is filled with He gas at 1 atm. As Inner Vessel shell is cooled to 80 K, the He gas within the Inner Vessel circulates by natural convection to cool the instrument package down to 80 K.
3. Purge the LHe reservoir of Nitrogen with He gas and slowly fill with Lhe.
4. The Helium gas within the inner vessel will continue to Cool Experiment Instrument package and inner vessel down to <10 K by natural circulation within the inner vessel.
5. After Experiment Instrument package and inner vessel reach desired temperature < 10 K, pump down inner vessel to <10-9 torr and verify that the rate of rise is < tbd . A heat exchanger is required to warm up pumped He gas prior to entering the vacuum pump.
6. Fill Dewar Assembly LHe reservoir

Operation

1. Disconnect from ground support subsystems.
2. Verify that all instrumentation and equipment is working as designed
3. Configure valving and controls to operate in Launch mode.
4. Launch – rise to altitude
5. Power up Experiment – 1 hour before Float, experiment will draw tbd watts
6. Float through experiment operation

Temperature Control

During Startup, Experiment Instrument package cooldown is accomplished by natural convection of He gas within the inner vessel. If control is needed it can be accomplished by controlling the pressure within the inner vessel.

Depending on losses, from 200 to 400 liters of LN_2 and from 400 to 800 liters of LHe will be required to complete startup cooldown.

During operation – launch and rise to altitude, the temperature of the inner vessel will be controlled by the boiloff of LHe within the inner vessel reservoir.

During operation – launch and rise to altitude, the temperature of the Experiment Instrument package will be controlled by some conduction through the supports and radiation heat transfer to the inner vessel surfaces.

During operation – float through Experiment, the temperature of the Experiment Instrument package will be controlled by radiation heat transfer to the inner vessel surfaces.

Initial Hardware Subsystem Description

Inner Vessel & Helium Reservoir

The LHe inner vessel is located and completely surrounded by the LN_2 shield/reservoir and its accompanying thermal isolation shield located just below it. Between the helium and nitrogen section will be a set of MLI blankets. The LHe reservoir portion of the inner vessel will be constructed in the shape of double walled cylinder containing LHe in the lower portion of the double wall. This vessel will be formed in two parts, the upper vessel, which will fit entirely within the upper section of the vacuum chamber, and inside the LN_2 reservoir and the lower section. A flange is located on the lower section of this vessel that will mount securely via hardware joining it to the bottom of the upper section. This will be joined to assure a good vacuum seal under cryogenic conditions. This lower head will form an isothermal intercept for protection of the lower internal chamber from incident radiation.

The inner vessel assembly will be designed for 16 psia internal and 0 psia external pressure.

The material used in the fabrication of this vessel will be type 304 stainless steel. Dimensionally the vessel will have an inside diameter of 100 cm (39.4 in.), an outside diameter of 109.2 cm (43.00 in.), and a height of 200.00 cm (29.00 in.).

Exiting from top of this vessel is a set of three fill and three vent tubes to allow filling of vessel itself. These three tubes will provide the structural support for the vessel as well. At the top of each tube a Goddard type of fitting will be located. This will allow the use of bayonet type fill systems and when not in use provide a means of closing off the access tubes. The volume potential of the vessel will be 254 liters of LHe. This is considerably larger than may be required for operation but will allow reduction at a later date.

The upper section of this vessel will have support points for the mounting of the experiment.

The entire helium reservoir and the lower shield will be wrapped in a blanket layer of 25 or more sheets of multi-layer insulation in order to further isolate any radiation loads from entering the helium storage vessel. This blanket will also be strategically slashed so as to avoid entrapment of air while evacuation is in process.

At all protrusions that pass through to the inner liquid helium vessel we will locate a set of thermal anchors to intercept the conductive heat load that will be traveling from the outside world into the helium vessel.

Liquid Nitrogen Shield/Vessel

The liquid nitrogen shield/vessel is the second wall to be encountered once inside the vacuum chamber. It will be constructed in the shape of hollow cylinder. This vessel will be formed in two parts, the upper vessel which will fit entirely within the upper section of the vacuum chamber, and they contain the LN_2 reservoir. The lower section will be fabricated in a simple top hat configuration seen in an inverted position. A flange is located on this lower vessel that will mount securely via bolts to the bottom of the upper section and will thermally joined by thermal grease to assure good contact. This lower inverted top hat will form an isothermal intercept for protection of the lower internal chamber from incident radiation.

Exiting from top of this vessel are a set of three fill, and three vent, tubes to allow filling of vessel itself. These tubes will also provide the structural support for the vessel as well. At the top of each tube a Goddard type of fitting will be located. This will allow the use of bayonet type fill systems and, when not in use, provide a means of closing off the access tubes. The volume potential of the vessel will be 46 liters of LN_2. This is considerably larger than will be required for operation but will allow reduction at a later date. The LN_2 shield/vessel will be contained entirely within the upper section of the Dewar.

The material used in the fabrication of this vessel will be 6061 – T6 aluminum or its equivalent. Dimensionally the vessel will have an outside diameter of 120.8cm (47.562 in.), an inside diameter of 116.5 cm (45.90 in.), and a height of 200.00 cm (78.74 in.). Located at the base of this vessel will be a set of threaded holes to which the lower shield will be mounted.

Because the LN_2 shield/reservoir is constructed of aluminum and the the vacuum vessel is stainless steel, an "aluminum to stainless" transition will be required to form an integral vacuum tight vessel. The tubes in a tubular configuration with a pant leg transition between the LN_2 and outer shell will provide more than adequate strength and vacuum integrity for this application. When the design is finalized we may wish to decrease the number of these tubes which will not affect the thermal or strength characteristics.

Attached at the base of the LN_2 reservoir will be a hemispherical thermal shield made of welded aluminum. The top flange of this shell will attach to the base of the LN_2 reservoir through a flange with the use of stainless steel hardware and will conduct any radiation generated in, and at, this shield up into the liquid nitrogen reservoir. This will maintain the temperature of this shell at a constant temperature, near 77K, presenting a radiation intercept point for absorbing radiation coming in from the outside (ambient) world.

The entire nitrogen reservoir and lower shield will be wrapped in a blanket layer of 25 or more sheets of multi-layer insulation in order to further isolate any radiation loads from entering the nitrogen storage vessel. This blanket will be strategically slashed so as to avoid entrapment of air while evacuation is in process. Otherwise this trapped air may lead to substantially large pockets of trapped air posing and showing up as virtual leaks as well as causing extended pump downs.

Outer Vessel

The Dewar will be split into an upper and a lower section. The two sections will be joined at flanges with an o – ring of sufficient cross section to ensure its capability of meeting and sustaining the vacuum requirements of the project. The upper section which is approximately TBD in height containing the cryogen containment vessels and the structural and electrical interconnects for the instrument package, and instrumentation for monitoring the Dewar conditions.

The lower half of the Dewar will be a simple sealed shell in which the lower section of the isothermal shield and lower section of the helium chamber shall be contained. The bottom head will be hemispherical. There will be no contact between these items and the Dewar wall in order to avoid thermal shorting.

The materials used for the construction of the Dewar outer shell shall be of type 304 stainless steel and of all vacuum welded construction. The cylindrical shape shall be capped at the upper section by an elliptical head through which access to the fill and vent for the LHe and LN_2 vessels will pass. This head will also provide the support for the Helium and LN_2 vessels.

The joining flange where the upper and lower section of the shell meets shall be constructed of 33.9mm (.75 in.) thick 304 stainless steel. The o-ring used for sealing the upper and lower sections shall be located at the flange on the lower section of the Dewar

The cylinder wall of the Dewar shall be fabricated from 304 stainless steel that will be rolled and full penetration welded. The shell wall will be welded to the top plate and at its base the flange where the upper and lower sections will join together. The welded assembly shall be fully leak tested to the required level to guarantee the integrity of the vessel. It may require the addition of stiffening rings in order to maintain its integrity and shape

In an effort to minimize the thermal radiation entering the vessel we recommend that the all outside surfaces be electropolished so as to minimize this potential heat load. Similarly the inner wall may be electropolished in an effort to minimize outgassing of the material and thereby avoid having to compensate for the potential loss of vacuum due to this characteristic.

Vacuum pumping ports

Pumping ports are required for the following volumes:

1. Annular space between the inner and outer vessel
2. Inner vessel
3. Ln_2 reservoir
4. Lhe reservoir

Cryogen Containment Chambers.

For this effort we have taken the approach that the chambers used for the Ln_2 reservoir as well as Lhe reservoir will be designed to utilize all the available space possible. We did this so as to have the latitude to reduce the volumes as needed once the design phase has been finalized. For this reason the vessels are substantially larger than need be while allowing for the impact of any undiscovered issues.

Valving to Allow Vapor Cooling after Launch

Located at the top of the Ln_2 reservoir just inside the vacuum vessel we are planning to locate a set of valves. These will be cryogenically rated valves and will be sealed where the actuators protrude up and through the top of the vacuum vessel. One valve (V1) will be located between the LN2 vent port tube and the fill port tube of the helium vessel. A second valve V2 will be located at a position between valve V1 and the He fill port. A third valve V3 will be located on the He fill tube located above the TEE connecting from valve V2 enabling an isolation of the helium fill tube.

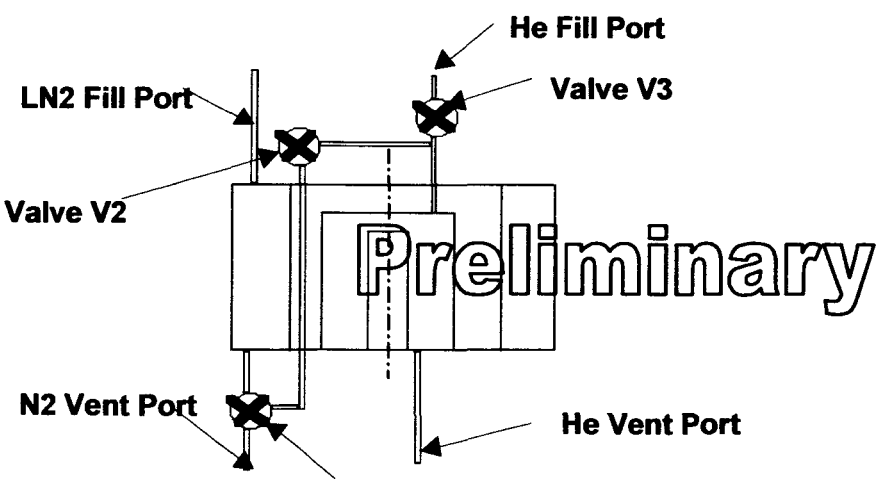

Vapor Cooling Schematic Diagram

During the initial fill and cool down of the system valve V1 would be closed, valve V2 would be open and Valve V3 would be closed. This would channel the cold nitrogen boil off gas to circulate into and through the Helium reservoir and perform an initial cool down of this vessel. By monitoring the temperature at the helium vessel until it begins to stabilize the operator can tell the condition of the vessel. Trying to force liquid helium into a room temperature vessel can result in a very violent reaction and should not be attempted and the temperature should be allowed to stabilize at as low a temperature as it can go.

The operator may then close valve V2, open valve V1, nitrogen vent port valve, couple the bayonet into the Goddard type fitting at the helium fill port, open valve V3 and commence filling the liquid helium vessel.

Another valve, not shown on the Schematic, could be located at the helium gas vent port and a line routed to enter into the instrument chamber.

The valves that are cryogenically rated will be positioned between the isothermal shield and the inside surface of the upper portion of the vacuum vessel. They are designed to keep the heat leaks low and vacuum tight. The actuating knobs would be accessible in the ambient condition or if desired we could design an electronic actuating system and keep the valves completely inside the vacuum space. While this might be more expensive it may be worth considering so that a completely hands off system would be feasible.

Open Issues or Risks:

1. The Inner Vessel Cryogenic Vacuum seal.
2. Symmetric design of Dewar System
3. Inner vessel and LN_2 shield support design
4. Control of the support of the Experiment Instrument package from room temperature, through cooldown, and cold operation.
5. Material to use for the inner vessel, LN_2 shield, and outer vessel. Materials discussed in the Initial Hardware Subsystem Description above are one possibility.
6. Accuracy required in weight distribution
7. Controlled cool-down with poor mixing and low velocity within inner vessel
8. Pump-down of the inner vessel after the inner vessel has been cooled to <10 K.
9. Assurance that the Experiment Instrument package has no 'pockets" of He, or (other contaminant) gas remaining after pump-down.
10. Heat leak at Experiment Instrument package support
11. Control of Experiment Instrument package temperature during launch and float (during experiment operation) Power required for Experiment Instrument package and power ON cycle.
12. The external configuration of the instrument package has not been finalized. The final design of this package has the potential to affect the thermal, mechanical, and vacuum conditions the Dewar is subjected to.
13. The interface of the Dewar to the balloon has not yet been determined and could potentially have an impact on our design philosophy as well as the structural integrity of the chamber.
14. The number and size of any electrical and/or mechanical feed-throughs past the vacuum wall has yet to be determined.
15. The size and configuration needs of the tubular access from the outside of the vessel into the inner chamber. We will also need its location in the vertical distance from the top of the Dewar.

Attachments

1. Baseline Conceptual Design Sketch

2. Plan and cost for engineering effort on Preliminary Design and Baseline Conceptual System cost -

Baseline Conceptual Design Sketch

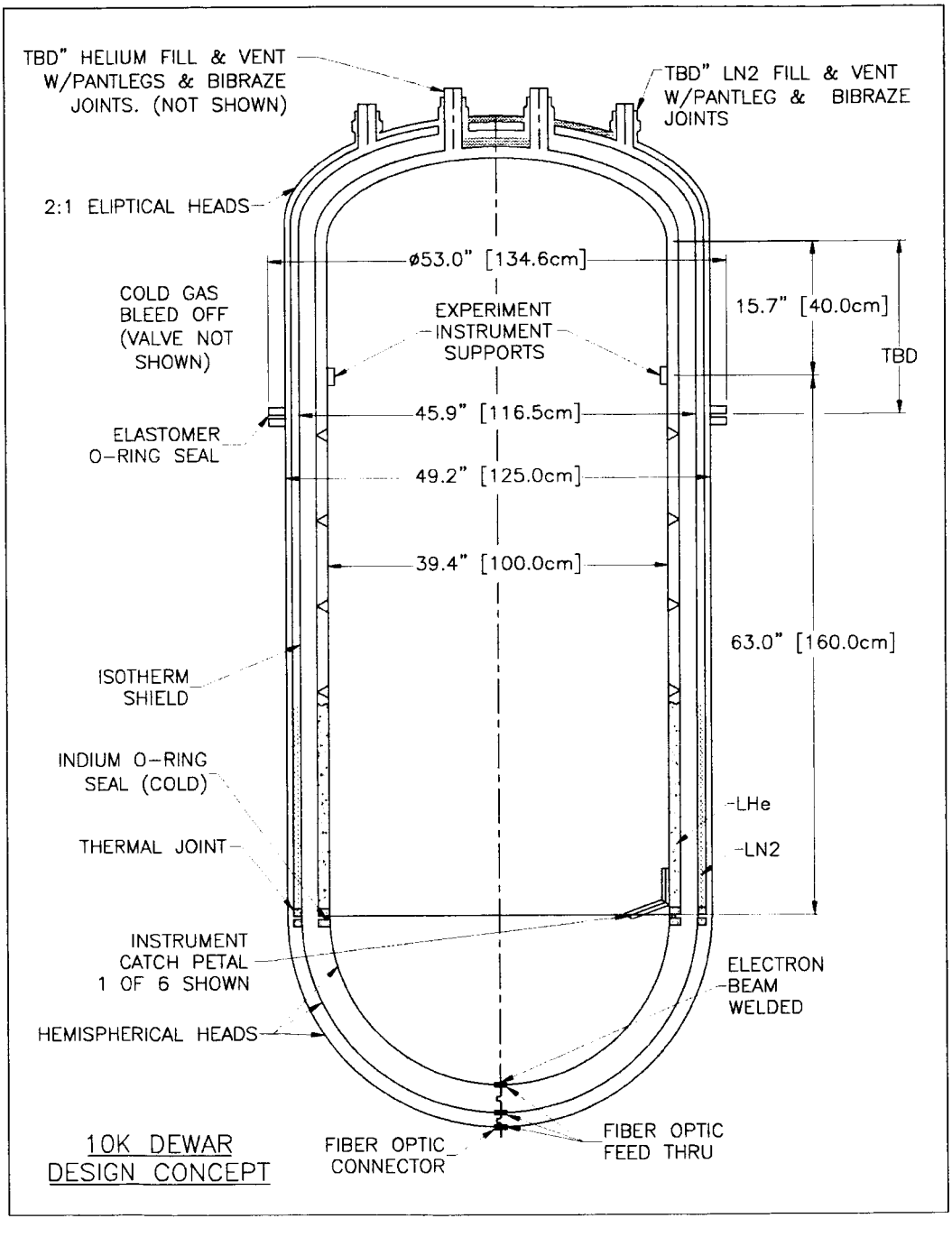

Figure 36 Design concept of cryostat

TO: Peter Cheimets

FROM Bill Bell

DATE: 12 March 2004

SUBJECT: Costing

The estimate below is for budget purposes only.

Engineering of Dewar and supporting equipment. Preliminary and Detailed Equipment Cost

Dewar

Vacuum pumping Skid – Insulating Vacuum 10-5 torr and Inner Dewar vacuum 10-9 torr. Inner Dewar vessel will contain Helium gas that is cold during pumping.

Cooldown We should be able to rely on natural convection. The He Dewar shell and LHe volume are first cooled down. He gas inside inner vessel circulates within inner vessel, cooling on upper surfaces and circulating down the walls and then up the core/center of vessel (vessel assumed to be vertical) where it cools the experiment. This continues until experiment reaches desired 10 K. This cold gas is then pumped out and warmed prior to entering vacuum pumps.

Cryogen Storage

LHe Dewar – 500 l

LN2 Dewar – 500 l

Piping

Instrumentation/Control - Vacuum and temperature

Assembly Test Startup

Budget Cost Estimate		
Item	Description	Estimate
1	Engineering of Dewar and supporting equipment. Preliminary and Detailed.	60 to 80K
2	Dewar	40K
3	Vacuum pumping Skid	40K
4	Cryogen Storage	
5	LHe Dewar	55K
6	LN2 Dewar	30K
7	Piping	5K
8	Instrumentation/Control	10K
9	Assembly Test Startup	20K
	Total	260 to 280K

Note: The Dewar prices assume purchase and they could be leased for a much lower cost.

References

[i] I.I. Shapiro et al., "Test of the Equivalence Principle in an Einstein Elevator." Final Report on NASA Grant NAG8-1780, April 2004.

[ii] I.I. Shapiro et al., "Test of the Equivalence Principle in an Einstein Elevator." Annual Report #2 on NASA Grant NAG8-1780, pp 82-85, June 2003.

[iii] Alvin L. Morris, (Editor), "Scientific Ballooning Handbook". NCAR Technical Note NCAR-TN/IA-99, 1975.

[iv] I.I. Shapiro et al., "Test of the Equivalence Principle in an Einstein Elevator." Annual Report #1 on NASA Grant NAG8-1780, pp 52-54, May 2002.